Ocean Modelling 70 (2013) 221–245

Contents lists available at SciVerse ScienceDirect

Ocean Modelling

journal homepage: www.elsevier.com/locate/ocemod

Global dynamical projections of surface ocean wave climate for a future high greenhouse gas emission scenario

Mark A. Hemer [a,*], Jack Katzfey [b], Claire E. Trenham [a]

[a] *CSIRO Wealth from Oceans National Research Flagship and the Centre of Australian Weather and Climate Research: A Partnership between CSIRO and the Bureau of Meteorology, GPO Box 1538, Hobart, TAS 7001, Australia*

[b] *The Centre of Australian Weather and Climate Research: A Partnership between CSIRO and the Bureau of Meteorology, Aspendale, VIC, Australia*

ARTICLE INFO

Article history:
Available online 17 October 2012

Keywords:
Surface ocean waves
Climate change
Dynamical projections
Wind-wave climate

ABSTRACT

A global 1° implementation of the spectral wave model, WaveWatch III, was forced with surface winds from two atmosphere–ocean general circulation models (AOGCMs: ECHAM5 and CSIRO Mk3.5), dynamically downscaled to 60 km using the Cubic Conformal Atmospheric Model. Two 30-yr time slices were simulated: 1979–2009 representing current climate, and 2070–2099 representing a future climate scenario under a high greenhouse gas emission scenario (SRES A2). A further wave model simulation with forcing from the NCEP Climate Forecast System Reanalysis for 1979–2009, using the same model settings as the climate model forced runs, serves as a benchmark hindcast to assess skill of climate-model-derived wave fields. Climate model forced wave simulations for the 1979–2009 time-slice display biases relative to the benchmark wave climate – notably an overestimation of wave generation in the Southern Ocean, which influences broad regions of the Pacific which receive these waves as swell. Wave model runs were repeated following bias-adjustment of the climate model forcing winds with the aim to reduce biases, but model skill to simulate the monthly 99th percentile of significant wave heights deteriorates severely.

Projected future changes in wave climate (between 1979–2009 and 2070–2099) under the SRES A2 greenhouse gas emission scenario are relatively insensitive to whether bias-adjustment of winds has been applied. Two robust features of projected change are observed from the two climate model sets which are qualitatively consistent with previous studies: a projected increase of Southern Ocean wave generation leading to approximately 10% increase in Southern Ocean mean significant wave heights (H_{Sm}), and a projected decrease in wave generation in the North Atlantic, with changes in H_{Sm} of similar magnitude.

Interannual anomalies of monthly mean significant wave height, H_{Sm}, were regressed against climate indices (Southern Oscillation Index – SOI; North Atlantic Oscillation – NAO and the Southern Annular Mode – SAM) over each time-slice. Significant differences in the relationships between wave height variability and these climate indices between current and projected climates are observed. For example, a significant shift from negative to positive correlation between the NAO and H_{Sm} anomalies along the western European and north-west African coasts in the projected future climate is noted. The potential future changes in wind-wave characteristics, and the changing relationships between interannual variability of wave climate with identified climate indices, as a response to projected future climate scenarios have broad implications for a range of processes and activities in the coastal, near-and-off-shore environments.

1. Introduction

There is increasing evidence for historical variability and changes in surface ocean wave climate. Studies using satellite altimeter data have described trends and variability in wave heights since at least the early 1990s (Hemer et al., 2010a; Young et al., 2011; Izaguirre et al., 2011), and studies based on the visual observing ship records suggest these trends extend over longer historical time periods (Gulev and Grigorieva, 2004). Observed changes in the wave height distribution are likely accompanied by changes in wave period and direction, as suggested by wind-wave reanalyses (Hemer et al., 2010a), and these combined influences will shift the equilibrium state of the coast. Furthermore, changes in wave climate will influence engineering requirements for offshore infrastructure (Weisse et al., 2008), and given the primary role of waves in the interactions which occur across the air–sea boundary, might also be expected to contribute to feedbacks in the coupled climate system (Cavaleri et al., 2012).

* Corresponding author. Tel.: +61 3 62325017.
E-mail address: Mark.Hemer@csiro.au (M.A. Hemer).

1463-5003/$ - see front matter
http://dx.doi.org/10.1016/j.ocemod.2012.09.008

Having identified the wind-wave climate responds to climate variability and the potential impacts of such changes, the research community have increased their efforts to understand how wave climate might be influenced under the effects of projected future climate change (Hemer et al., 2012c). These efforts have had a predominantly regional focus, which potentially overlooks regions of the global ocean/coast of greater risk – whether measured as a function of magnitude of hazard (amount of wave climate change), or as function of vulnerability (with regions of lower adaptive capacity at greater risk; Hemer et al., 2010b). The Pacific Islands, where waves have a strong influence on marine and coastal infrastructure and ecosystems and associated economic resources, are a notable region of potential high risk to future change in wave climate. Similar arguments apply for many other nations globally, reflecting a need for a global understanding of the wave climate response to projected future changes in climate.

Hemer et al. (2012a, 2012b) used a limited ensemble of surface winds derived from a regionally downscaled climate model (RCM), to determine the magnitude of projected change in wave climate for the east coast of Australia for two future greenhouse gas emission scenarios. They assessed the benefit of adjusting the RCM surface winds to minimise bias with respect to NCEP Reanalysis-2 winds, to improve representation of the regional wave climate. In this study, we apply the same approach to determine two realisations of the global wave climate response under a single projected future (SRES A2) high greenhouse gas emission climate scenario. The spaectral wave model, WaveWatch III (v3.14, Tolman, 2009) is dynamically forced using surface winds derived from the Cubic-Conformal Atmospheric Model (CCAM, McGregor, 2005; McGregor and Dix, 2008), which has downscaled two CMIP-3 general circulation models (CSIRO Mk3.5 and ECHAM5) to approximately 0.5° resolution globally. The runs are repeated with climate model surface winds adjusted to minimise bias with respect to the NCEP Climate Forecast System Reanalysis using the method proposed by Hemer et al. (2012), to determine benefit of this procedure to represent the current global wave climate.

It is well established that interannual wave climate variability responds to large scale changes in atmosphere–ocean systems. Correlation of interannual anomalies of monthly mean significant wave height with climate indices representing these systems has been used widely to determine these relationships. For example, wave climate variability in the Pacific Ocean varies with the El-Niño – Southern Oscillation (ENSO), indicated by strong correlations with the Southern Oscillation Index (SOI) or similar ENSO indicator (e.g., Niño3.4 index) (e.g., Gulev and Grigorieva, 2004, Izaguirre et al., 2010, Hemer et al., 2010a). In turn, the associated wave climate variability has been noted to influence shoreline position along the eastern Australian coast (Short and Trembanis, 1994; Short et al., 2000, Ranasinghe et al., 2004; Harley et al., 2011) and the western coast of North America (Storlazzi and Griggs, 2000; Allan and Komar, 2006). Similarly, wave height variability in the North Atlantic Ocean varies strongly with the North Atlantic Oscillation (NAO) (Woolf et al., 2002, Izaguirre et al., 2010), with an associated coastal response (Thomas et al., 2011). An analysis of satellite altimeter wind-wave data and the ERA-40 reanalysis found the principal component of variability of Southern Hemisphere wave climate was significantly correlated with the Southern Annular Mode (SAM), particularly during the austral winter months (Hemer et al., 2010a). These studies aim to understand the relationships of wind-wave climate variability to large-scale climate phenomena in order to provide predictive capacity on seasonal and climatological time-scales. There is a consequent need therefore to establish whether dynamical wind-wave variability will relate to these climate indices in the same manner in a future climate scenario as in the present climate.

Our study has three aims: (1) Identify how well the present global wave climate is represented using a dynamical downscaling approach from two CMIP-3 GCMs (and whether bias-adjustment of surface winds can improve this); (2) Determine the magnitude of projected change in wave climate for a single, high (SRES A2) greenhouse gas emission scenario; and (3) identify whether the relationship between dynamical wind-wave variability and key climate indices (SOI, SAM, NAO) remains the same under a future climate scenario.

2. Data

2.1. ERA-Interim

ERA-Interim is the latest global atmospheric reanalysis produced by the European Centre for Medium Range Weather Forecasts (ECMWF; Dee et al., 2011). ERA-Interim spans the period January 1, 1979 onwards, and continues to be extended in near-real time. The 31-yr period, 1979–2009 inclusive, is used for this study. At the time this study commenced, ERA-Interim archives included 3-hourly surface wave parameters (significant wave height, H_S, mean wave period, T_M, and mean wave direction, θ_M) on a 1.5° latitude–longitude grid. ERA-Interim wave parameters are derived from a fully coupled atmosphere–wave model (WAM) which describes the evolution of two-dimensional wave spectra at the sea-surface, with satellite radar altimeter-derived wave height data (from 1991 onwards) used to adjust the model predicted wave spectra based on assumptions about the contributions of wind-sea and swell. The wave model is applied with a horizontal resolution of 110 km, with wave spectra discretised using 24 directions and 30 frequencies. The model includes several enhancements over the version used in ERA-40, including a reformulation of the dissipation source term and introduction of a scheme to parameterise unresolved bathymetry. Notable improvement of ERA-Interim wave parameters (H_S, T_M, and T_P) relative to ERA-40 were observed by Dee et al. (2011), with the overall quality of ERA-Interim wave fields being equivalent to the operational analysis of 2005. Here we use the 1.5° resolution ERA-Interim dataset, freely available to the research community, to define a point of reference surface wind and wave climate derived from the 31-yr record for comparison.

2.2. NCEP Climate Forecast System Reanalysis

The US National Centre for Environmental Prediction (NCEP) Climate Forecast System Reanalysis (NCFSR; Saha et al., 2010) was designed and executed as a global, high resolution coupled atmosphere–ocean–land surface–sea ice system to provide the best estimate of the state of these domains over the period January 1979 to present. This reanalysis does not include ocean waves, but provides a high resolution (spatial – 0.5°, and temporal – hourly) representation of near-surface marine winds globally which represents all but the most intense tropical and extratropical storms with high skill (e.g., Cox et al., 2011). Here the NCFSR near-surface winds are used as a benchmark dataset for climate model derived winds, and as forcing for a 31-yr wave hindcast using the same model parameterisations used for the climate model forced runs.

2.3. CCAM downscaled GCM surface winds

The World Climate Research Programme (WCRP) endorsed Working Group on Coupled Modelling (WGCM) established the Coupled Modelling Intercomparison Project (CMIP) as a protocol for investigating output of coupled atmosphere–ocean general circulation models (AOGCMs). Phase 3 of CMIP (CMIP-3; Meehl et al.,

2007) provided much of the data underpinning the Intergovernmental Panel on Climate Change (IPCC) Fourth Assessment Report (AR4; IPCC, 2007). The CMIP-3 data comprise output from 25 AOGCMs, however these models are implemented at coarse resolution (mean spatial resolution of 2.1°), and surface winds were not archived at sufficient temporal resolution to support dynamical wind-wave studies. Dynamical wave studies are strongly dependent on the quality of the forcing surface winds. These must be archived at high spatial and temporal resolution to adequately represent storm wind systems so that realistic wave fields can be generated within the model. For this study, we use dynamically downscaled climate model outputs obtained from CSIRO's Cubic Conformal Atmospheric Model (CCAM; McGregor and Dix, 2008), which was used to dynamically downscale two CMIP-3 GCM runs (CSIRO Mk3.5 and ECHAM5) for a single, high (SRES A2) greenhouse gas emission scenario. The two models were chosen as representing a medium and high climate change response to future emission scenarios. The global surface temperature climate change response from CSIRO Mk3.5 is approximately equal to the CMIP3 ensemble mean. ECHAM5 has one of the highest simulated changes in surface temperature over the 21st century. CCAM is a full atmospheric GCM formulated on the conformal-cubic grid. CCAM was applied globally with a resolution of approximately 60 km, and 18 vertical levels. Forcing is derived from sea-ice and sea-surface temperatures from the parent AOGCMs, which have been bias-adjusted using a simple additive approach (detailed by Katzfey et al., 2011) to reduce large SST biases seen in the AOGCMs (i.e., there are no atmospheric forcings from the AOGCMs; Katzfey et al., 2011). Three-hourly near-surface (10-m) winds and daily sea-ice concentrations, spanning the period 1960–2100, archived on a 0.5° global grid were available from the two CCAM runs. This study considered two time-slices of 30-yr or more from these records, representing a current climate (1979–2009) and a future climate (2070–2099).

Two GCMs were downscaled to explore the range of possible conditions associated with multi-model ensembles in the projected climate. This ensemble is too limited to provide an adequate estimate of the uncertainty within the total sample space if all 25 AOGCMs were considered. The study did not consider uncertainty associated with emission scenarios, intra-model ensembles, or between downscaling models. The choice to limit the ensemble to two members was based on two factors: (a) computational limitations; and (b) the downscaling step using CCAM reduces the spread of surface wind field scenarios which are observed in the forcing AOGCMs.

Biases in distribution of wind speed and direction (mean climate and variance biases) were found between the CCAM derived surface winds and the NCFSR surface winds. Following Hemer et al. (2012a), a bivariate quantile adjustment of CCAM winds was carried out, which adjusts both directional components of the surface wind field to align in distribution with the NCFSR winds. It extends the widely used quantile adjustment procedure to a vector variable (surface wind) to adjust biases in the mean and variability of the CCAM derived wind fields. Wind speed and direction are adjusted by dependently mapping the joint probability distribution (JPD) of eastward (u) and northward (v) wind components onto the JPD of u and v from the NCFSR winds dataset at each grid cell. Firstly the u wind component is distributed into percentile bands, at 2 percentile intervals (i.e., adjustment of maximum values follow adjustments of all values between the 98th percentile and the maximum value), leading to a 50×1 adjustment vector for u at each grid cell. Within corresponding u percentile bands from the CCAM and NCFSR datasets, the empirical distributions of v are determined. A quantile adjustment (at 2 percentile intervals) of the CCAM empirical v distribution (within the given u percentile band) is made to fit the corresponding NCFSR empirical distribution (a 50×50 adjustment matrix for v at each grid cell is determined). Two sets of adjustment matrices are produced – one for each CCAM wind dataset (the CSIRO Mk3.5 and ECHAM5 forced runs), providing a two-member ensemble of bias-adjusted CCAM derived surface winds, for each time-slice. i.e.,

$$u_{\mathrm{cor},x,i} = u_{1,x,i} + M_{u,x,i}, \tag{1}$$

$$v_{\mathrm{cor},x,y,i} = v_{1,x,y,i} + M_{v,x,y,i}, \tag{2}$$

where u_1 and v_1 represent eastward and northward CCAM derived wind components respectively, $M_{u,x,i} = u_{2,x,i} - u_{1,x,i}$ and $M_{v,x,y,i} = v_{2,x,y,i} - v_{1,x,y,i}$, are the bias adjustment matrices, where u_2 and v_2 represent eastward and northward NCFSR derived wind components respectively, x denotes the xth percentile of the eastwards wind u-component, y denotes the yth percentile of the northwards wind v-component within the xth u-component, and i denotes location. To investigate wind changes over future time periods, the projected future CCAM winds are adjusted using the corresponding model adjustment matrices evaluated from the historical time-slice (i.e., assume the model biases are time invariant) as investigated by Hemer et al. (2012b).

To summarise, for each time-slice, four forcing wind datasets are used: un-adjusted winds derived directly from two CCAM runs (CSIRO Mk3.5 and ECHAM5 forced runs); and bias-adjusted winds from two CCAM runs.

3. Methodology

3.1. Wave modelling

This study has investigated wave climate model skill with forcing derived from downscaled CMIP-3 experiments. Our approach follows the dynamical method outlined by Hemer et al. (2012a, 2012b), but extended to a global domain (summarised in Fig. 1). The WaveWatchIII wave model (version 3.14, Tolman, 2009) was implemented over a near-global domain (latitude 80°S–80°N) at 1° spatial resolution. Despite surface winds being available at higher resolution, the wave model was limited to 1° spatial resolution on the basis of reducing required computational resources (computing time and storage). The $1° \times 1°$ model grid is defined using the automated grid generation software for WaveWatch III (Chawla and Tolman, 2007) using the DBDB2 v3.0 bathymetry, and GSHHS shoreline database, defining an obstruction grid for unresolved boundaries in the sub-grid domain. The wave spectra of the WaveWatch III model was defined by a directional resolution of 15° and 25 frequency bands ranging non-linearly from 0.04 to 0.5 Hz. On the basis of early CFSR forced runs, WaveWatch III was implemented using the WAM4 parameterisations as adapted by Bidlot et al. (2007, referred to as BAJ in the WaveWatch III manual).

A total of nine wave model runs were carried out (Table 1). These included five runs spanning the historical period 1979–2009, and four spanning 2070–2099 representing a future climate under the SRES A2 greenhouse gas emission scenario.

Spanning the period 1979–2009, run *G1d_cfsr* was forced using NCFSR near-surface winds and sea-ice concentrations. This run serves as a benchmark global hindcast, using the same model grids and parameterisation, to assess skill of the climate model forced wave fields. We deem the climate model forced runs to be acceptable if model skill is comparable to the *G1d_cfsr* run.

For each time-slice, two runs are carried out forced with downscaled climate model near-surface winds directly. For the 1979–2009 period, these are *G1d_mk3.5_20c* and *G1d_echam5_20c*, which are forced with CCAM winds downscaling the CSIRO Mk3.5 GCM and the ECHAM5 GCM respectively. These runs together form a

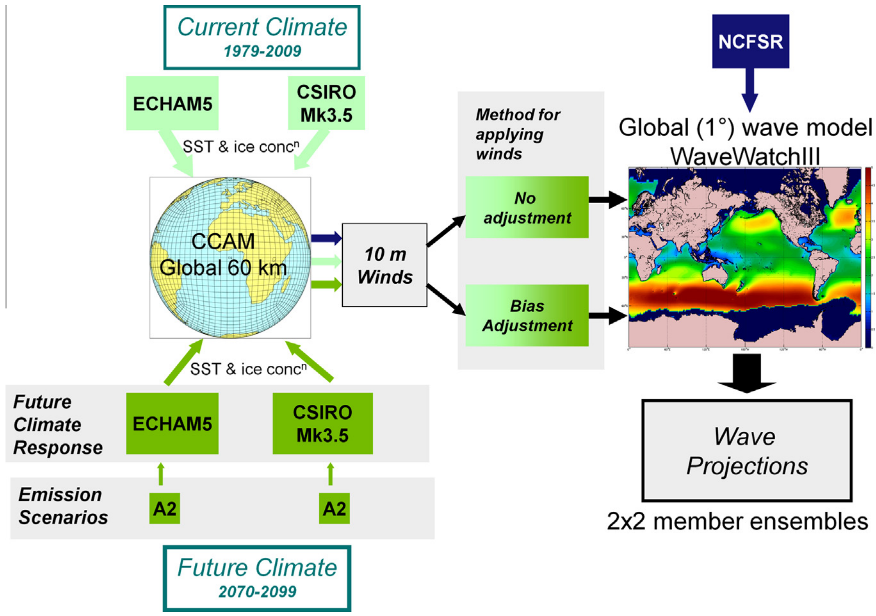

Fig. 1. Schematic of dynamical wave climate modelling methodology used in this study.

Table 1
List of model runs carried out in this study.

Ensemble	Model run	Run period	CCAM forcing	Bias-adjusted winds
G1d_cfsr	*G1d_cfsr*	1979–2009	–	No
G1d_ens_20c	*G1d_mk3.5_20c*	1979–2009	Mk3.5	No
	G1d_echam5_20c	1979–2009	ECHAM5	No
G1d_ens_21c	*G1d_mk3.5_21c*	2070–2099	Mk3.5	No
	G1d_echam5_21c	2070–2099	ECHAM5	No
G1d_ba_ens_20c	*G1d_ba_mk3.5_20c*	1979–2009	Mk3.5	Yes
	G1d_ba_echam5_20c	1979–2009	ECHAM5	Yes
G1d_ba_ens_21c	*G1d_ba_mk3.5_21c*	2070–2099	Mk3.5	Yes
	G1d_ba_echam5_21c	2070–2099	ECHAM5	Yes

2-member current climate ensemble: *G1d_ens_20c*. For the 2070–2099 period, the corresponding runs are *G1d_mk3.5_21c* and *G1d_echam5_21c*, and the 2-member future climate ensemble: *G1d_ens_21c*. In addition, for each time-slice, two wave model runs are carried out where forcing is derived from the same downscaled climate model runs, with near-surface winds bias-adjusted to have a distribution aligned with NCFSR. For the 1979–2009 period, these runs are *G1d_ba_mk3.5_20c* and *G1d_ba_echam5_20c*, and a 2-member ensemble referred as: *G1d_ba_ens_20c*. For the 2070–2099 period, the corresponding runs are *G1d_ba_mk3.5_21c* and *G1d_ba_echam5_21c*, with the two member future climate ensemble: *G1d_ba_ens_21c*. The wave model runs forced with bias-adjusted winds were carried out to determine whether global wave model skill can be improved using the approach described by Hemer et al. (2012a, 2012b).

3.2. Analysis procedure

Our primary interest is the mean wave climate and seasonal cycles described by each model run. Our analysis derives 4 monthly parameters from each model run: monthly mean significant wave height, H_{Sm}; the monthly 99th percentile of significant wave height, H_{Sm99}; monthly mean wave period, T_{Mm}; and monthly mean wave direction, θ_{Mm}. These parameters are determined for each model grid cell for each month, leading to 372 time-series points for each cell within the 161×360 model grid. These monthly parameters are determined for each of nine model runs outlined in Table 1. The same parameters are derived from the 1979–2009 ERA-Interim wave database for comparison.

We compare annual means of each monthly parameter from run *G1d_cfsr* against ERA-Interim globally. Similarly, we compare seasonal means (December to February mean representing boreal winter, and June to August mean representing boreal summer). We then compare the results of each CCAM forced wave model run with run *G1d_cfsr* for same periods. Projected change in each wave parameter is determined by the difference between the future 30-yr mean, and the corresponding current climate 30-yr mean of the given parameter. The significance of the projected changes is assessed using a standard *t*-test for difference in means.

3.3. Interannual variability

Inter-annual wave climate variability is dependent on large-scale changes in the atmosphere–ocean system. Previous studies have identified significant relationships between wave height variability and other regional climate patterns around the world. In this study we are interested in whether relationships between wave climate and large scale climate indices (SOI, NAO and SAM) are observable in the climate model derived wave climate, and whether these relationships are maintained in the future wave climate. To investigate, we regress the derived wave climate against these climate indices. We determine the three climate indices (SOI, NAO and SAM) from the mean sea-level pressure record of each CCAM run directly. For simplicity, we use the same form to approximate each index, analogous to the Troup SOI (Troup, 1965), as the standardised anomaly of the mean sea level pressure (MSLP) difference between two given regions. The indices are calculated as:

$$Index = 10(\Delta P - \Delta Pm)/SD(\Delta P),$$

where ΔP is the difference between monthly averaged MSLP at region 1 and the monthly averaged MSLP at region 2. Subtracting ΔPm, the mean annual cycle of ΔP, removes the mean annual cycle from ΔP. $SD(\Delta P)$ is the long term standard deviation of ΔP for the given month of year. A value of -10 means the index is 1 standard deviation on the negative side of the long-term mean for that month. Using this definition for all indices results in each index (particularly NAO and SAM) having a value which is an order of magnitude larger than is common.

To determine SOI, the pressure difference is determined between Tahiti and Darwin, consistent with the Troup definition. The NAO is determined using the same form, with the pressure difference between Lisbon, Portugal and Reykjavik, Iceland used. Derivation of a SAM index also follows the same form, except the pressure difference is determined between the zonal mean MSLP at 40°S and the zonal mean MSLP at 65°S. Indices (SOI, NAO and SAM) are determined from the NCFSR dataset for the period 1979–2009, and from each CCAM model (Mk3.5 and ECHAM5) for time-slices 1979–2009 and 2070–2099. Indices corresponding to the bias-adjusted CCAM winds are not available – MSLP is not altered in the bias-adjustment procedure. Finally, the 12 month running mean of each detrended index is regressed against the 12-month running mean of wave height anomaly (monthly mean wave height with the mean annual cycle subtracted, and detrended) from each wave model run, with significance tested using a *t*-test statistic to determine whether the regression slope differs significantly from zero. To examine whether changes in regression coefficients between climate indices and H_{Sm} anomalies in the projected future climate are significantly different from the current time-slice, we use a bootstrap method (Efron, 1982). We repeat the calculation of regression coefficients 500 times, with repeat random sampling with replacement of the H_{Sm} anomalies. We are then able to construct a probability distribution function for regression coefficients at each grid cell, from each wave model run. Regions with significant future changes in regression coefficients are those where no overlap of the central 95% of the PDF (between 2.5% and 97.5% probabilities) is observed between the present and future time-slice distributions. These regions are interpreted as having significantly different relationships between the given climate index and wave climate under the future climate scenario.

4. Results

4.1. Present climate

4.1.1. Marine Surface Wind Speeds (U10)

Fig. 2 displays the annual and seasonal zonal mean surface wind speed from the two CCAM runs (CCAM-echam5 and CCAM-mk3.5). We define the zonal mean surface wind speed at each parallel of latitude, as the mean surface wind speed across all ocean longitudes at the given latitude. Surface winds derived from these two models are in close agreement across the global ocean. This limited range of variability within the CCAM ensemble follows the results of Hemer et al. (2012a), where it was shown the GCM downscaling approach using CCAM markedly reduced the spread of surface wind speeds seen within the forcing GCM ensemble.

The spatial resolution of ERA-interim winds is coarser than the CCAM and NCFSR winds, and as a result is not able to resolve the position of maxima to the same degree as the higher resolution models. Despite this, we observe better agreement between the CCAM surface winds and ERA-Interim than between the CCAM and NCFSR winds. Consistent with the results presented by Hemer et al. (2012a), the climate model derived winds exaggerate the zonal flow relative to the benchmark (ERA-Interim and/or NCFSR) winds. This is more notable relative to ERA-interim winds, which we attribute to the resolution issue mentioned above. A positive bias in zonal mean wind speeds is observed in each of the northern and southern extratropical storm and trade wind belts (Fig. 2). These positive biases are more apparent during the corresponding hemispheric winter. For example, climate model wind speeds are overestimated in the Southern Ocean storm and southern trade belts during the austral winter (JJA; Fig. 2(c)), but show good agreement with ERA-Interim during the austral summer (DJF, Fig. 2(b)). Difference between reanalyses winds (ERA-Interim and NCFSR) however are greater than the difference between CCAM and either reanalysis – CCAM wind speeds being typically bounded by reanalysis winds (i.e., overestimate ERA-Interim winds, and underestimate NCFSR winds). This providing additional confidence in the quality of CCAM winds for the study.

The CCAM model winds suggest evidence of an expanded Hadley cell in both hemispheres (Fig. 2(a)), indicated by a poleward bias in the position of the wind speed minima corresponding to the position of the subtropical ridge. This bias is more apparent during the boreal winter mean (DJF, Fig. 2(b)) in both hemispheres, and is not observed during the boreal summer mean (JJA, Fig. 2(c)). Bias-adjustment of the surface wind fields, following the method proposed by Hemer et al. (2012a) removes these biases in the mean wind field. The bias-adjusted winds align with the NCFSR winds in Fig. 2 by definition.

The monthly 99th percentile of wind speed ($U10_{99}$, not shown) displays the same properties as the mean wind speed discussed above. Zonal mean values of the monthly 99th percentile are dominated by peaks in the extratropical storm belts, with a southern peak annual mean of approximately 20 m/s and 18 m/s from the climate models and ERA-Interim respectively, and a northern peak showing greater agreement between the CCAM runs and ERA-Interim with values of approximately 17 m/s.

4.2. Wind-waves

4.2.1. NCFSR forced hindcast

The structure of the global wave climatology has been well described in several previous studies (e.g., Young, 1999; Sterl and Caires, 2005). While the structure of the significant wave height climatology is well represented by the *G1d_cfsr* run, relative to ERA-Interim *G1d_cfsr* annual mean significant wave heights display a positive bias over large portions of the global oceans (Fig. 3). This bias is approximately 10–15% in the extratropical regions, and slightly lower (<5%) in the tropical Atlantic and western tropical Pacific oceans. A larger positive bias (up to 20%) relative to ERA-Interim is observed in the eastern tropical Pacific. Fig. 4 shows the zonal mean H_{Sm} for the period 1979–2009. Seasonal mean significant wave heights show overestimation of wave heights is greater during winter months, with higher positive biases recorded in the north Pacific and Atlantic basins during the boreal winter months (DJF, Fig. 4(b)). In the Southern Ocean, a positive bias is observed for all seasons. However, higher positive biases in H_{Sm} are observed during the austral winter months (JJA, Fig. 4(c)). The positive biases observed in H_{Sm} are similarly represented in H_{Sm99}, with maximum bias of approximately 20% observed in the extratropical storm belts.

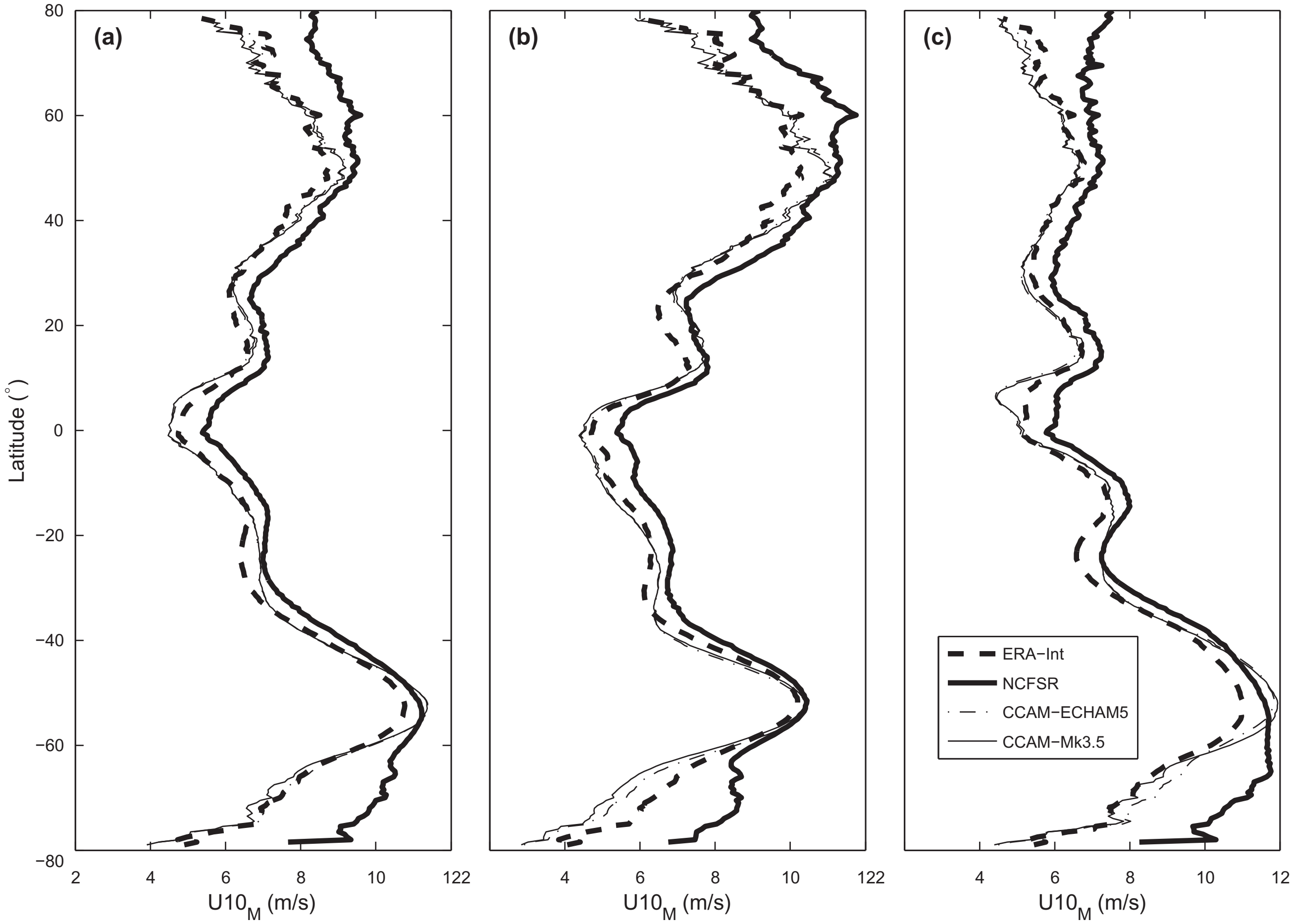

Fig. 2. Zonal mean near-surface wind speed, U10, for the period 1979–2009 (m/s). (a) Annual mean; (b) Dec–Feb mean; and (c) Jun–Aug mean. Close agreement between CCAM models is observed by overlaying lines.

Fig. 5 shows the zonal mean, T_{Mm} for the 1979–2009 time-slice. Mean wave period shows similar structure to prior climatologies (e.g., the web-based KNMI/ERA-40 wave atlas described by Sterl and Caires, 2005), but a long bias of *G1d_cfsr* derived mean wave periods with respect to ERA-Interim is observed throughout the global ocean. This bias is largest, with magnitudes of approximately 1 s, in the swell dominated regions of the global ocean such as the tropical Indian and eastern Pacific oceans, and is high (approximately 0.5 s) throughout the Southern Hemisphere (not shown).

Fig. 6 shows the zonal mean θ_{Mm} for the period 1979–2009. Biases in θ_{Mm} between *G1d_cfsr* and ERA-Interim are typically less than 10°, except localised occurrences where steep gradients in wave direction are observed, such as the subtropical divergence zones (not shown). The differences in these regions may be attributed to the coarse resolution of the 1.5° resolution ERA-Interim product, shifting relative position of these features by a grid cell. This agreement of wave direction in the *G1d_cfsr* run relative to ERA-Interim is within the 15° resolution of the wave model, and shows the *G1d_cfsr* run is a suitable benchmark for this study.

4.2.2. Forcing with surface winds directly from downscaled climate models

When the WaveWatch III wave model is forced with CCAM derived near-surface winds, the global spatial variability of the annual mean wave climate, described in prior studies (e.g., Young, 1999) is reproduced. The zonal mean H_{Sm} from runs *G1d_echam5_20c* and *G1d_mk3.5_20c* display good agreement (|bias| < 0.2 m) with run *G1d_cfsr* and ERA-Interim across all latitudes, except the Southern Ocean storm belt (Fig. 4). A negative bias of approximately 0.4 m is observed in the North Pacific between longitudes 100–250°E (Fig. 7(a) and (b)). A notable positive bias of similar magnitude in the annual mean H_{Sm} relative to *G1d_cfsr* is observed in the Southern Ocean over the same longitude range (Fig. 7(a) and (b)). This is balanced by a slight negative bias relative to *G1d_cfsr* over remaining longitudes, so the Southern Ocean storm belt zonal mean of the annual mean H_{Sm} aligns with *G1d_cfsr* (Fig. 4(a)). During the austral summer (DJF, Fig. 4(b)), the zonal mean H_{Sm} from runs *G1d_echam5_20c* and *G1d_mk3.5_20c* more closely align with ERA-Interim in the Southern Hemisphere, having a negative bias with respect to *G1d_cfsr*. During the austral winter however (JJA, Fig. 4(c)), the climate model derived wave fields display a strong positive bias (of more than 1 m relative to ERA-Interim, and 0.25 m relative to *G1d_cfsr*) in the Southern Hemisphere. The positive bias in the Southern Ocean extends into the eastern tropical Pacific, particularly during the austral winter (not shown). Tropical regions elsewhere exhibit a negative bias (<10%) in H_{Sm}. The spatial structure of biases is consistent for both H_S statistics assessed (H_{Sm} and H_{Sm99}), and percentage bias magnitudes are similar (not shown).

The spatial variability of mean wave period from runs *G1d_echam5_20c* and *G1d_mk.5_20c* reflects previous climatologies. Relative to run *G1d_cfsr*, a negative bias of up to 0.5 s in annual mean T_{Mm} is observed over all regions except regions

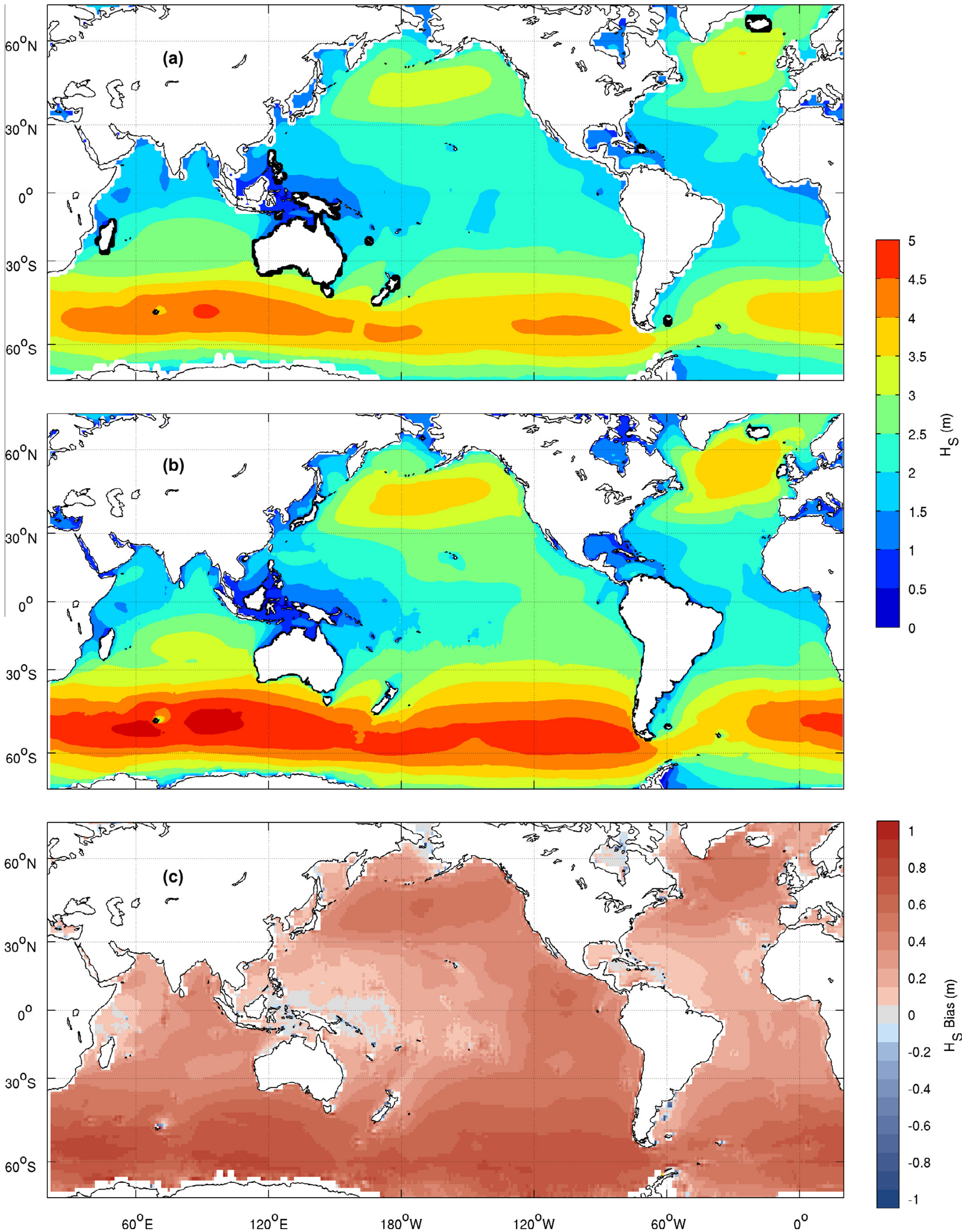

Fig. 3. (a) Mean annual significant wave height (m), H_S, from ERA-Interim for period 1979–2009; (b) as for (a), from run *G1d_cfsr*; and (c) bias between *G1d_cfsr* and ERA-Interim derived mean annual H_S (m). Positive values indicate *G1d_cfsr* overestimates ERA values.

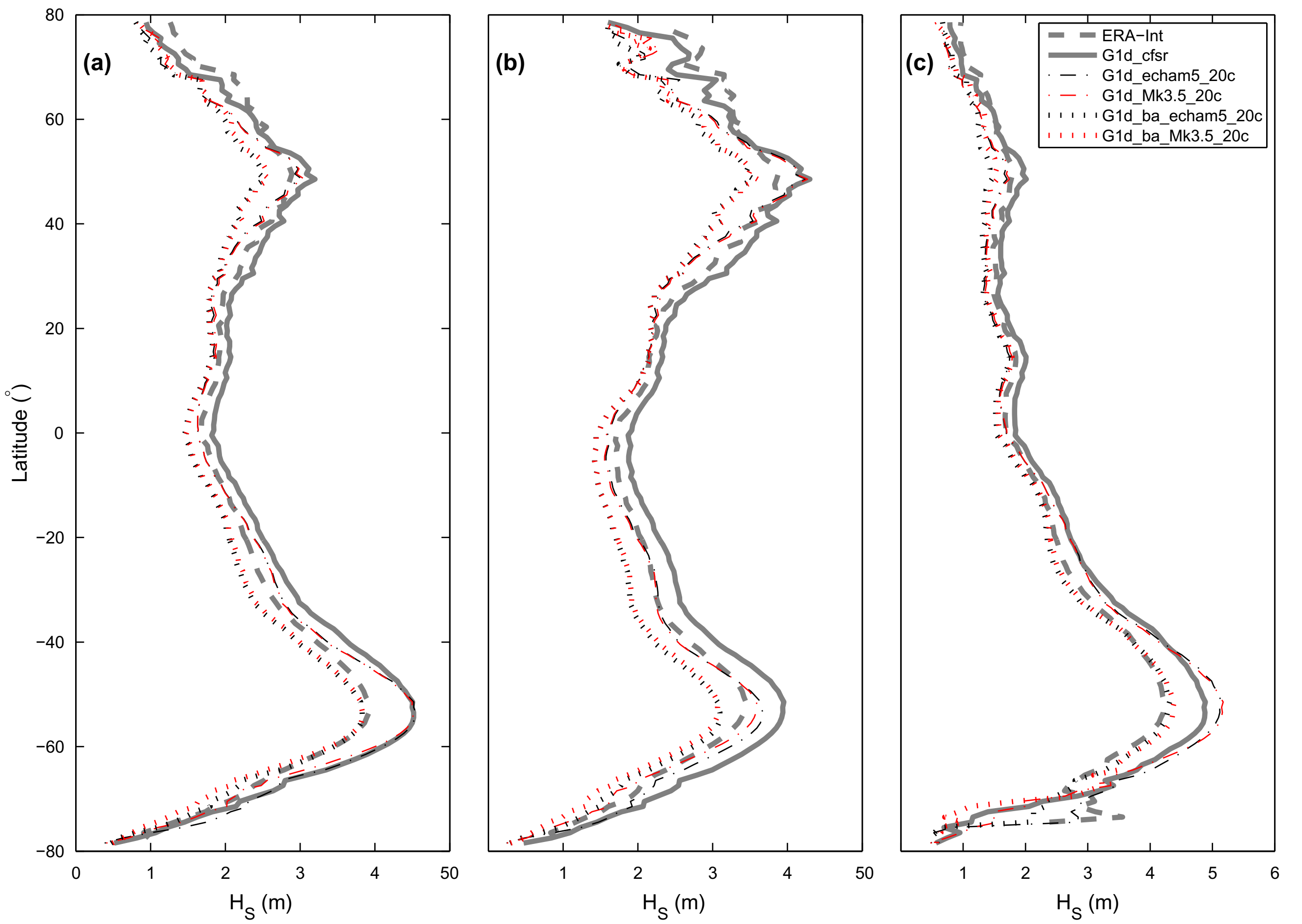

Fig. 4. Zonal mean significant wave height, H_S, for the period 1979–2009 (m). (a) Annual mean; (b) Dec–Feb mean; and (c) Jun–Aug mean. Close agreement between respective CCAM forced models is observed by overlaying lines.

corresponding with high swell energy (following distribution presented by Semedo et al., 2011), including the Southern Ocean and tropical eastern Pacific, which show good agreement with *G1d_cfsr* (Fig. 8). The negative bias observed relative to *G1d_cfsr* is greater in magnitude during the austral summer (seen in DJF zonal mean, Fig. 5(b)), with little bias in T_M observed during the austral winter (seen in JJA zonal mean, Fig. 5(c)). Recalling the bias between *G1d_cfsr* and ERA-Interim, the regions of negative bias between the CCAM forced runs and *G1d_cfsr* show relatively close agreement with ERA-Interim, while regions of small bias in the tropical eastern Pacific and eastern Indian Oceans translate as a strong positive bias relative to ERA-Interim (in excess of 1 s in mean annual T_{Mm}).

Mean wave direction within the CCAM forced runs displays similar structure to *G1d_cfsr* and ERA-Interim, but a bias towards more zonal wave directions in all regions of the global ocean is noted (Fig. 9). Easterly mean wave directions in the tropics (north-easterlies in the northern tropics, and south-easterlies in the southern tropics) have a greater easterly component in runs *G1d_echam5_20c* and *G1d_mk3.5_20c*, indicated by a bias of approximately 5°. To a lesser extent, westerly mean wave directions in the extra-tropics (north-westerly in the Northern Hemisphere, and south-westerly in the Southern Hemisphere) have a greater westerly component in runs *G1d_echam5_20c* and *G1d_mk3.5_20c*, with a directional bias of less than 2° (Fig. 9). This zonal bias remains present throughout the year, with the position of transition between positive and negative biases shifting with corresponding seasonal change in position of the subtropical ridge (Fig. 6).

4.2.3. Forcing with bias-adjusted downscaled climate model near-surface winds

Bias-adjustment of climate model derived forcing winds so that the bivariate distribution of surface winds in the 1979–2009 time-slice aligns with the NCFSR distribution has a large influence on the modelled wave field. In a general sense, the spatial variability of the global wave climate remains, but a strong negative bias with respect to run *G1d_cfsr* is observed globally, except the western tropical Pacific and the Gulf of Mexico (Fig. 7(c) and (d)). The zonal mean H_{Sm} from runs *G1d_ba_echam5_20c* and *G1d_ba_mk3.5_20c* display large negative biases (between 0.5 and 1.0 m) relative to run *G1d_cfsr* across all latitudes (Fig. 4). This bias remains relatively constant regardless of season. Notably, the large positive biases with respect to ERA-Interim in the Southern Ocean wave heights observed in runs *G1d_echam5_20c* and *G1d_mk3.5_20c* during the austral winter (JJA) is reduced to near zero for these runs with bias-adjusted forcing. A bias of approximately 0.35 m remains during the austral summer.

Large negative biases in wave heights in runs with bias-adjusted wind forcing are more apparent when looking at storm wave conditions (e.g., H_{Sm99}). Model skill in representing storm wave systems deteriorates severely for runs *G1d_ba_echam5_20c* and *G1d_ba_mk3.5_20c*. Looking at zonal mean H_{Sm99}, a negative bias relative to *G1d_cfsr* of approximately 4 m is observed in the

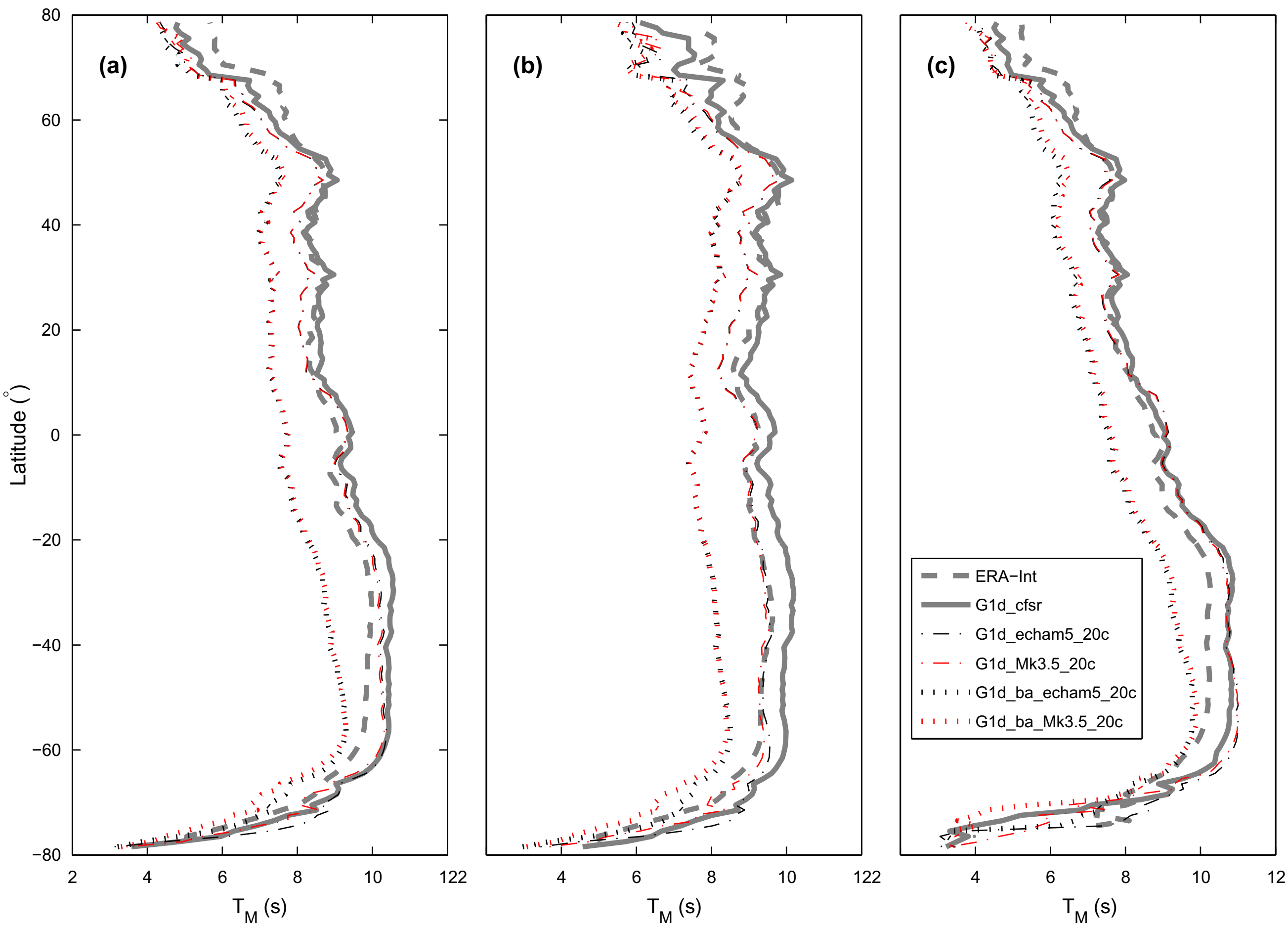

Fig. 5. Zonal mean, mean wave period, T_M, for the period 1979–2009 (s). (a) Annual mean; (b) Dec–Feb mean; and (c) Jun–Aug mean. Close agreement between respective CCAM forced models is observed by overlaying lines.

southern extratropical storm belt throughout the year (Fig. 10(a)–(c)), and in the northern extratropical storm belt in the boreal winter (Fig. 10(b)). These biases in storm wave conditions provide an explanation for the observed decrease in H_{Sm} in the runs with bias-adjusted forcing.

Reduced skill modelling storm wave systems carries through to also influence wave periods and directions. Runs *G1d_ba_echam5_20c* and *G1d_ba_mk3.5_20c* consequently show a strong negative bias in T_{Mm} (of between 1 and 3 s), relative to both *G1d_cfsr* and ERA-Interim, across the global ocean (Fig. 8). The bias is greater in regions with more relative swell energy (eastern tropical Pacific and Indian oceans). Relative to *G1d_cfsr*, the T_{Mm} bias remains relatively constant throughout the year (Fig. 5).

Changes in wave direction resulting from the bias-adjustment of forcing winds are observed as a further increase in the zonal bias in wave directions relative to run *G1d_cfsr*, particularly in the southern and northern tropics (i.e., more easterly component to the south-easterly and north-easterly winds, respectively, Fig. 9). This response is more pronounced during the boreal winter months (DJF, not shown), when observed in both hemispheres, but is also seen in the Southern Hemisphere during the austral winter (JJA). We attribute this directional response to the reduced influence of swell waves. Bias-adjustment of the wind fields limits generation of storm waves. It is these waves which propagate as swell into regions away from the storm belts. As a consequence, the observed mean wave direction becomes a function of local wind forcing only, and consequently a zonal bias in wave direction results.

4.3. Projected changes at the end of the 21st century

4.3.1. Marine Surface Wind Speeds (U10)

Projected changes in mean wind speed, determined as the difference between the 2070–2099 mean and the 1979–2009 mean, display differences between the two CCAM runs (CCAM-ECHAM5 and CCAM-Mk3.5). Two robust features are observed in the projected changes in wind speed in the CCAM runs: (1) weakening wind speeds in the Northern Hemisphere, particularly in the North Atlantic basin where significant projected decreases of approximately 3 m/s in the annual mean wind speed are observed, and (2) strengthening of the southern extratropical westerlies where a significant projected increase of approximately 1 m/s in annual mean wind speed is observed (Fig. 11). This projected strengthening is greater during the austral winter months.

The projected increase in Southern Ocean wind speeds is more uniform zonally, and spans a broader range of latitudes in the CCAM-ECHAM5 model than in CCAM-Mk3.5 (Fig. 11). South of 45°S, CCAM- increased wind speeds are projected by ECHAM5 almost uniformly for all longitudes (Fig. 11(a)). For the CCAM-Mk3.5 model, aside from the Pacific sector which is similar to CCAM-ECHAM5, the projected increase in Southern Ocean wind speeds is greater, but only observed further south (south of 55°S; Fig. 11(b)). In both models, the southern subtropics (25–45°S) are

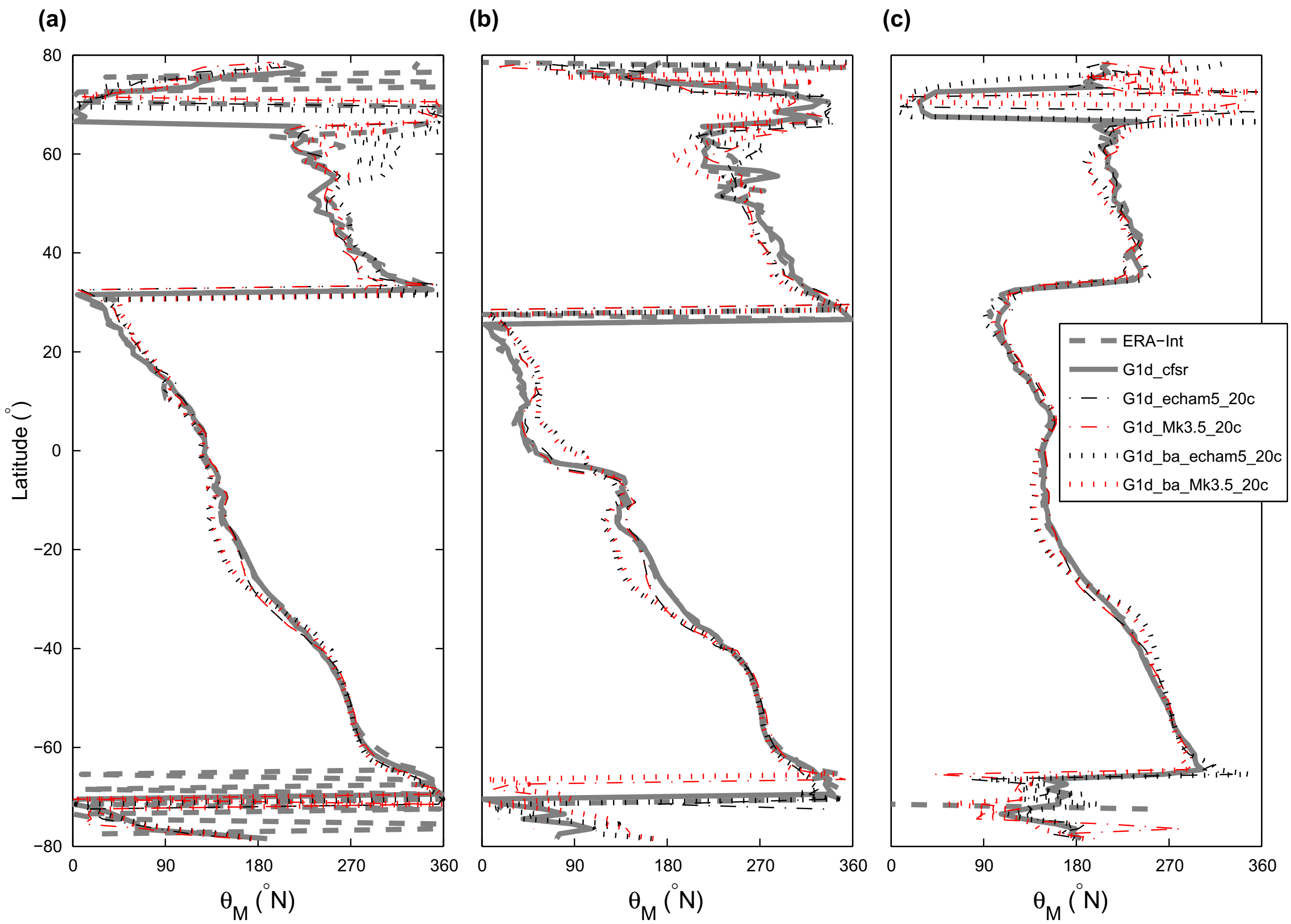

Fig. 6. Zonal mean, mean wave direction, θ_M, for the period 1979–2009 (°N). (a) Annual mean; (b) Dec–Feb mean; and (c) Jun–Aug mean. Close agreement between respective CCAM forced models is observed by overlaying lines.

a region of projected decrease in mean wind speed. In the southern equatorial Pacific, both models project strengthening wind speeds, although these are more extensive in the CCAM-ECHAM5 model (where strengthening extends from 170°E eastwards to the American continent) than in CCAM-Mk3.5 where the strengthening is localised to the central Pacific. In the Indian Ocean, a notable projected increase in wind speeds is observed in the eastern equatorial Indian during the dry season (JJA) which is stronger in the CCAM-Mk3.5 model (~2 m/s increase) than in CCAM-ECHAM5 (<0.5 m/s increase). In the region of calm prevailing winds at the intertropical convergence zone, a projected decrease of more than 1 m/s is observed in both models. In each model, the north-easterly Pacific trades display a southerly contraction with a projected increase in the south of the trade wind belt (significant in the CCAM-Mk3.5 model only) and a decrease of approximately 1–2 m/s in wind speed in the northern half of the north-easterly trade wind belt.

The projected change in bias-adjusted winds matches the projected changes in un-adjusted winds presented in Fig. 11.

4.3.2. Wind-waves

Here, we discuss only results taken from the model being forced with surface winds directly from the downscaled climate model. This follows the results presented in Section 4.1 which showed a deterioration of wave model skill when forced with bias-adjusted winds. We note however that the projected change signal from the runs with bias-adjusted forcing show close agreement with the projected change signal from runs with direct forcing (not shown).

The two robust features observed in the wind field (increasing westerlies in the Southern Ocean, and the weakening wind speeds in the North Atlantic) are observed in the projected changes in H_{Sm} (Fig. 12). In the Southern Ocean, particularly in the Pacific sector between latitudes 40°S and 60°S, a projected increase in wave heights of up to 0.4 m (~7%) is observed for the given future climate scenario. This region is also a region of strong bias in the climate model forced runs relative to the *G1d_cfsr*. Few locations display projected change in excess of the magnitude of the bias (Fig. 12). The projected significant increase in Southern Ocean mean wave heights is greatest during the austral winter months, with maximum projected increase (outside of ice affected areas) in H_{Sm} of almost 0.6 m observed SW of New Zealand at approximately, 50°S, 180°E (not shown). In the austral summer, a projected decrease in H_{Sm} of 0.2 m is observed between latitudes 30°S and 50°S. Reflecting the projected changes in wind speed, the projected increase in Southern Ocean wave heights spans a greater latitude range in CCAM-ECHAM5 forced runs, with projected significant increase in H_{Sm} as far north as the Tasman Sea, with a corresponding significant increase in wave heights in the eastern equatorial Pacific Ocean associated with an increase in the Southern Ocean generated swell component (Fig. 12(a)). In the CCAM-Mk3.5 forced runs, the projected increase in H_{Sm} is observed further south, with little increase in annual mean wave heights observed in the ice-free ocean (Fig. 12(b)). During the austral winter (JJA) however, significant increase in H_{Sm} is projected over a large area of the Southern Ocean, extending northwards into the Tasman Sea, from both models, with a corresponding increase

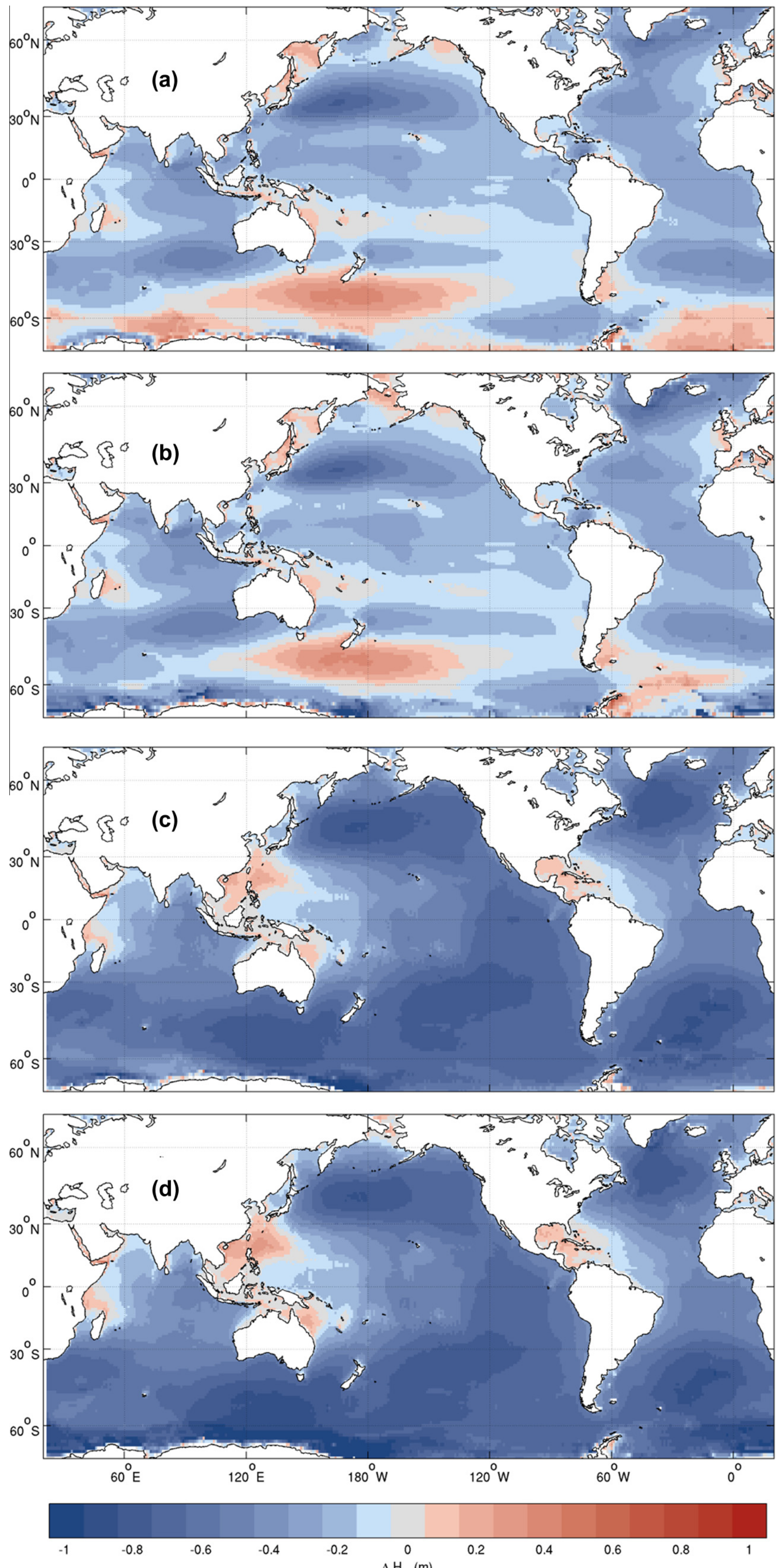

Fig. 7. Annual mean H_S bias with respect to run *G1d_cfsr* (m). (a) *G1d_echam5_20c*, (b) *G1d_mk3.5_20c*, (c) *G1d_ba_echam5_20c*, and (d) *G1d_ba_mk3.5_20c*. Positive values indicate the climate model forced runs overestimate *G1d_cfsr*.

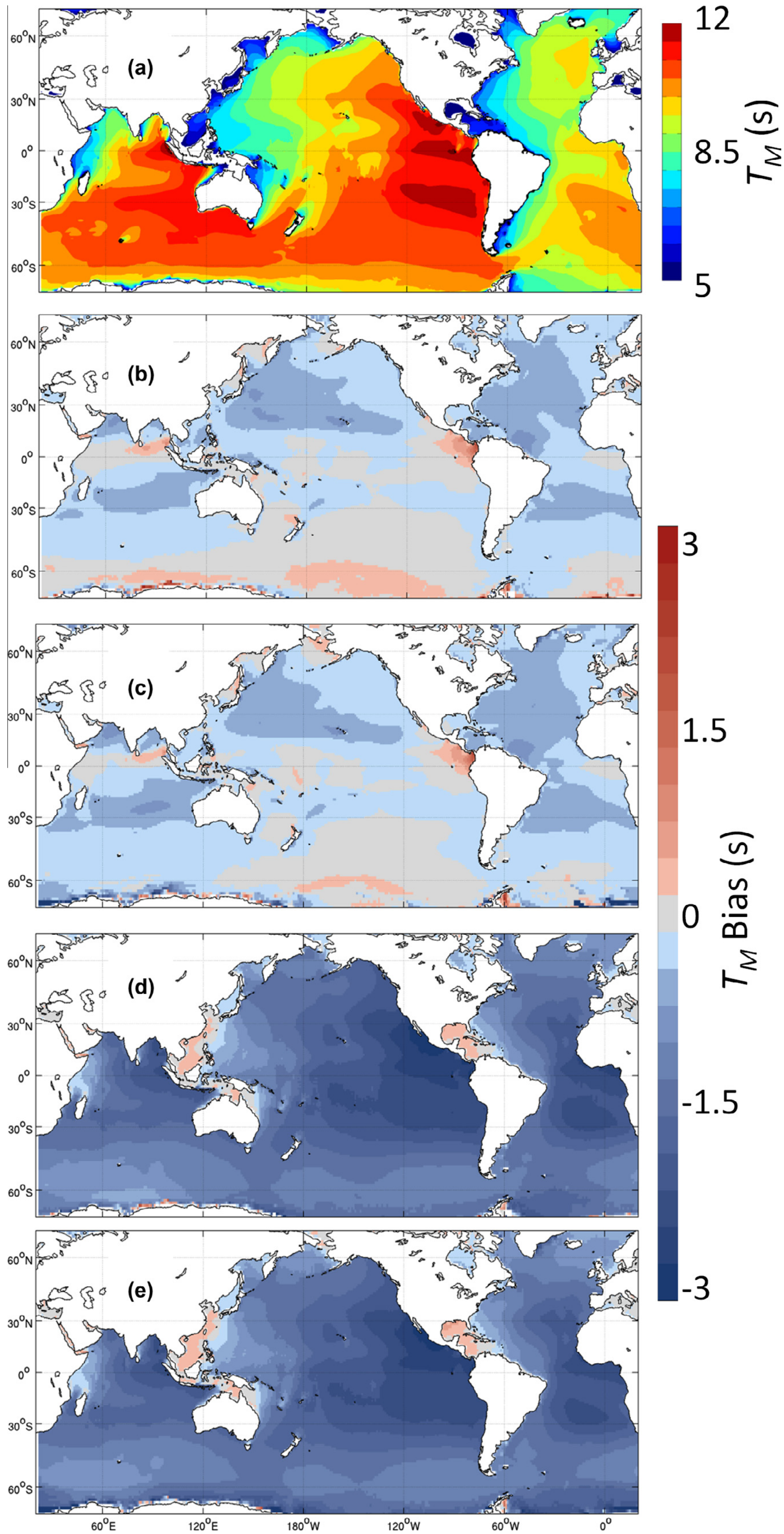

Fig. 8. (a) Mean annual T_M (s) from run *G1d_cfsr*. The following plots display annual mean T_M bias (s) with respect to run *G1d_cfsr*. (b) *G1d_echam5_20c*, (c) *G1d_mk3.5_20c*, (d) *G1d_ba_echam5_20c*, and (e) *G1d_ba_mk3.5_20c*. Positive values indicate the climate model forced runs overestimate *G1d_cfsr*.

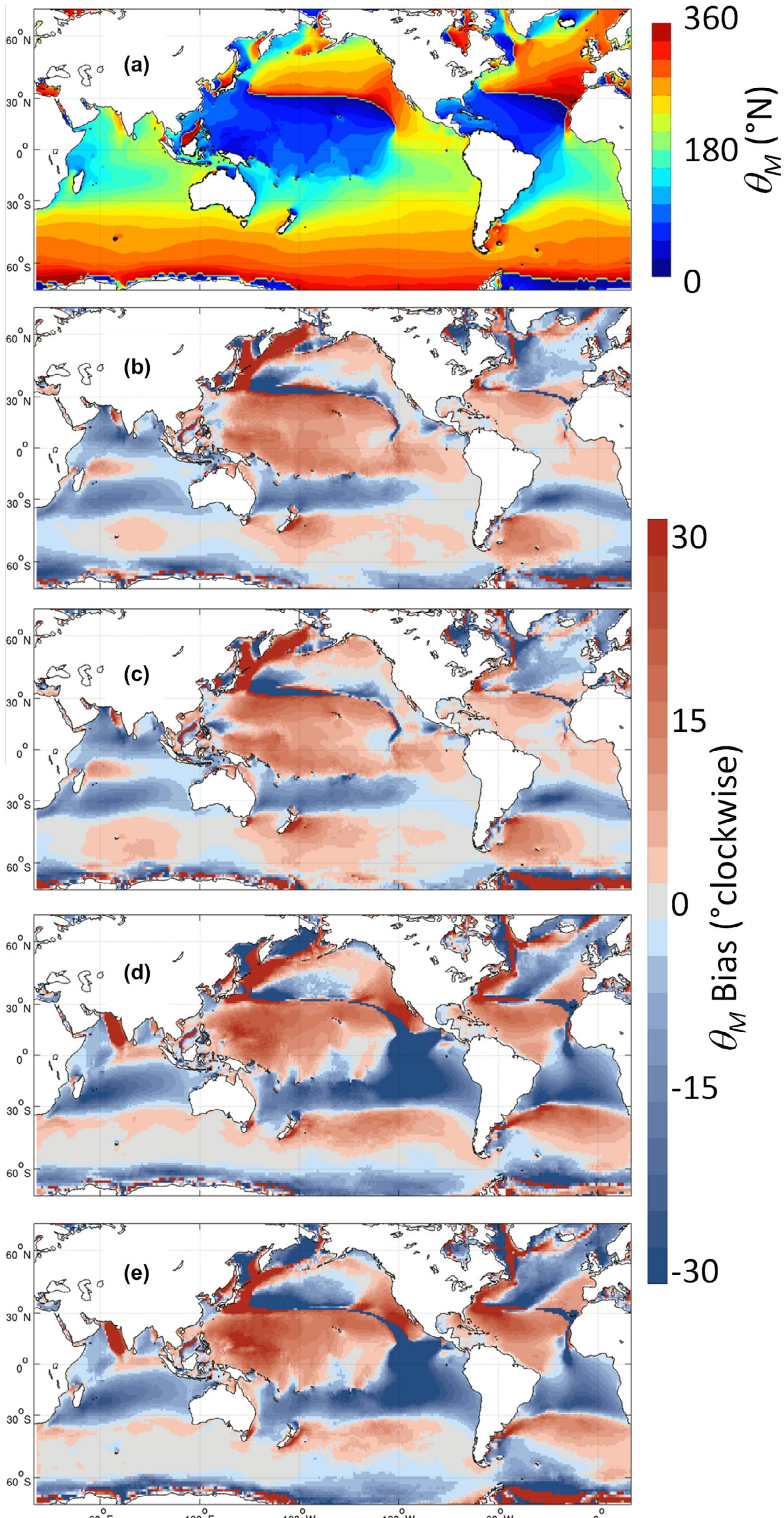

Fig. 9. (a) Mean annual θ_M (°N) from run *G1d_cfsr*. The following plots display annual mean θ_M bias (°clockwise) with respect to run *G1d_cfsr*. (b) *G1d_echam5_20c*, (c) *G1d_mk3.5_20c*, (d) *G1d_ba_echam5_20c*, and (e) *G1d_ba_mk3.5_20c*. Positive values indicate the climate model forced runs have a clockwise bias with respect to *G1d_cfsr*.

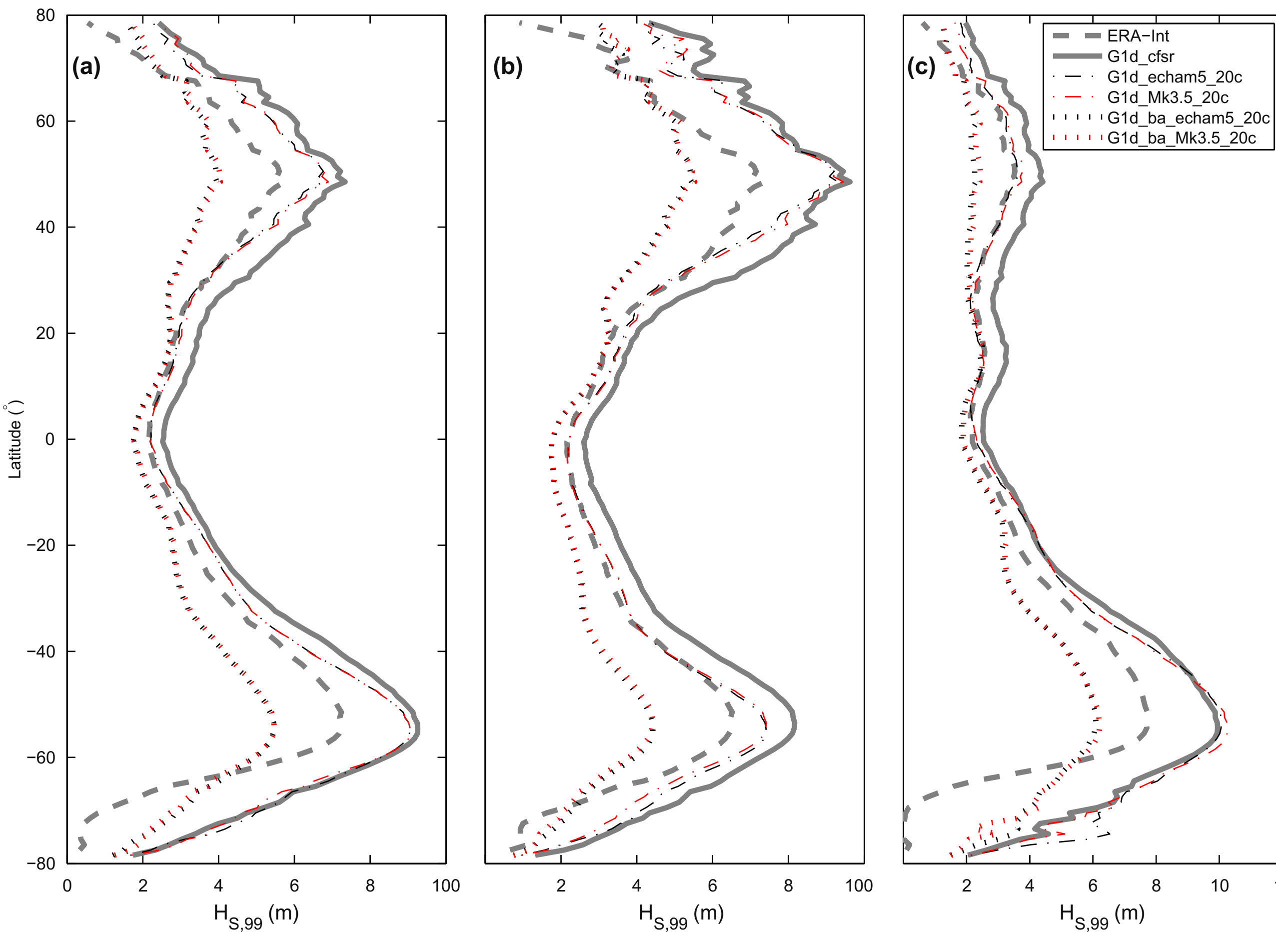

Fig. 10. Zonal mean monthly 99th percentile of significant wave height, $H_{S,99}$, for the period 1979–2009 (m). (a) Annual mean, (b) Dec–Feb mean, and (c) Jun–Aug mean. Close agreement between respective CCAM forced models is observed by overlaying lines.

in regions affected by Southern Ocean swell (eastern tropical Pacific, Indian and South Atlantic Oceans). These regions display a consequent significant increase in annual mean T_{Mm} of approximately 0.5 s.

A decrease of up to approximately 0.7 m (∼15%) in H_{Sm} is projected in the North Atlantic, with the maximum change observed at approximately 45°N, 30°W in the central North Atlantic. Similar projected decrease in H_{Sm} is observed in the North Pacific basin (Fig. 12(a) and (b)). Both the CCAM-ECHAM5 and CCAM-Mk3.5 forced wave fields show a projected decrease in H_{Sm} in the northwest Pacific and North Atlantic, which is stronger during the boreal winter (∼1 m decrease) than boreal summer (∼0.2 m decrease), and this seasonal variability is reflected in the zonal mean projected changes (Fig. 13). A corresponding significant decrease in T_{Mm} of approximately 0.5 s is observed in these regions.

Aside from the ice-influenced Sea of Okhotsk, Labrador Sea and Hudson Bay, projected change in H_{Sm} for the Northern Hemisphere up to the end of the 21st century is almost entirely decreasing. This is attributed to the widespread projected decrease in wind speeds across the Northern Hemisphere observed in Fig. 11. The observed projected decrease in wave heights in the north and east Indian Ocean are also consistent with local projected decreases in wind speed. The Southern Hemisphere shows greater variability, with a projected increase associated with the extratropical storm belt which extends northwards (contracts southwards) during the austral winter (summer).

The spatial distribution of projected changes in H_{Sm99} is very similar to the projected changes in H_{Sm} discussed above. The magnitude of projected change in the storm waves (99th percentiles) is larger than those for the mean wave heights by a factor of approximately 2.

The projected response in wave direction shows a general trend towards a greater southerly component to mean wave direction (∼3–5° directional shift) throughout the global ocean, with projected changes of up to 10° observed at some locations (Figure ure14). However, there are several locations where this general trend is not observed. These locations tend to be in regions of islands and/or complex topography, and diffraction/refraction processes influence the wave direction response. The subtropical ridge in each hemisphere appears to be a region of larger projected change in wave directions. We attribute this to the sensitivity of wave direction to the position of the ridge, which is projected to shift pole-wards in the future climate scenarios. No clear seasonal structure to the projected changes in wave direction is observed.

4.3.3. Interannual variability

This section investigates the interannual variability of only the wave model runs forced with un-adjusted CCAM surface winds. Figs. 15–17 show the results of the regression analysis of *G1d_ncfsr*, *G1d_echam5_20c* and *G1d_echam5_21c* derived H_{Sm} anomalies against the SOI, NAO and SAM climate indices, respectively, for both historical and future time-slices. The regression coefficient values plotted reflect the magnitude of the response of the annual mean H_{Sm} per unit of climate index (i.e., a value of 0.05 suggests a unit increase in the climate index is associated with a 5 cm increase in the annual mean H_{Sm} (e.g., a regression coefficient of 0.02 relative to SOI suggests an El Niño event (SOI < −10) is associated with a 20 cm negative anomaly of H_{Sm} at that given location).

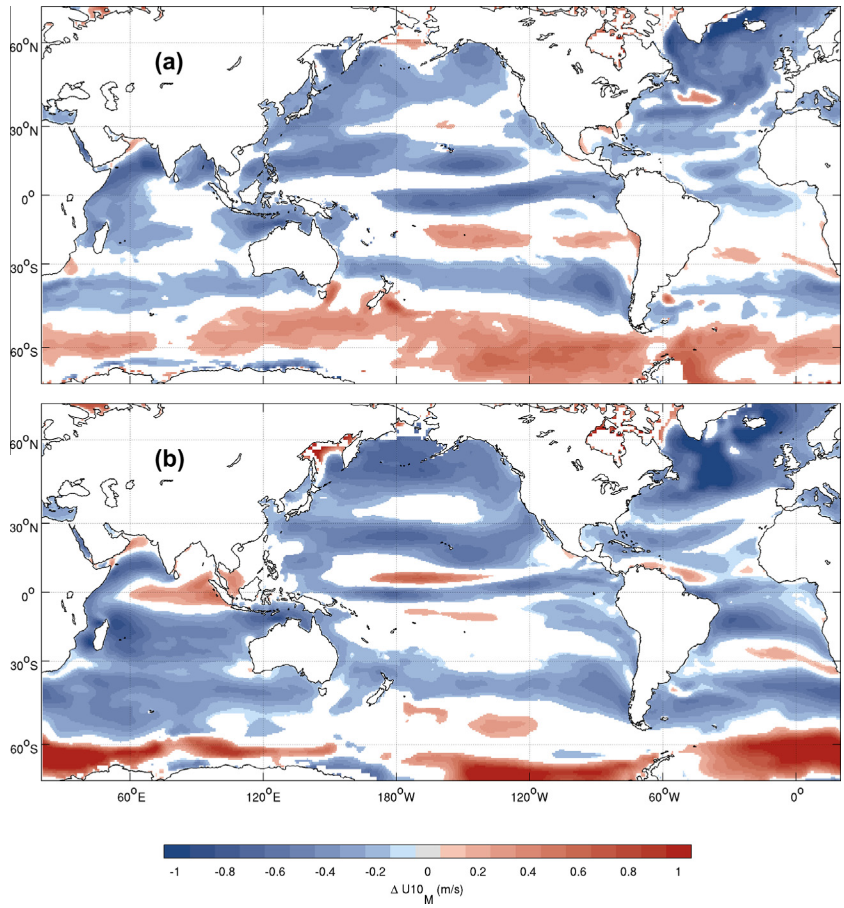

Fig. 11. Projected change (m/s) in annual mean near-surface (10 m) wind speed (2070–2099 less 1979–2009) for the SRES A2 scenario, from runs (a) CCAM-ECHAM5, and (b) CCAM-Mk3.5. Only regions where projected future annual mean wind speed is significantly different (at 95% confidence level) to historical annual mean wind speed are coloured. (For interpretation of the references to colour in this figure legend, the reader is referred to the web version of this article.)

Table 2 shows the range of climate index values in each dataset, according to the definition used in this study.

The regression coefficients of the H_{Sm} anomaly against the SOI for run *G1d_ncfsr* displays strongest relationship in the Pacific Ocean, displaying features consistent with prior studies (e.g., Laing, 2000; Hemer et al., 2010a; Izaguirre et al., 2010; Fan et al., in press; Figure 15(a)). A positive anomaly of the SOI (La Niña phase) is associated with decreasing wave heights over large portions of the Pacific, particularly in the south-west Pacific, consistent with prior studies, and in the Northern Hemisphere westerly storm belt. The well-documented positive correlation between H_{Sm} and the SOI in the Tasman and Coral seas on Australia's eastern coast (Ranasinghe et al., 2004; Short et al., 2000) and in the South China Sea are observed. Positive correlations are observed in the south-eastern part of the Pacific basin, with a strong H_S response observed in the Southern Ocean to the west of Chile. The region of positive correlation to the SOI adjacent to Australia's west coast noted by Hemer et al. (2010a) is also observed.

In runs *G1d_echam5_20c* and *G1d_mk3.5_20c*, representing the current time-slice using climate model forcings, we observe several of these same features in the corresponding map of regression coefficients (Fig. 15(b) and (d)). Strong negative relationships are observed over broad expanses of the Pacific Ocean, concentrated in the south-west Pacific and in the northern westerly storm belt (although distributed more evenly across the North Pacific). Regions of positive correlation are also observed in the south-east Pacific adjacent to the Chilean coast and in the Tasman and Coral Seas, although in run *G1d_echam5_20c* (Fig. 15(b)), the region of positive correlation in the Tasman region is weak and shifted eastwards to be centred north of New Zealand. The positive relationship in the South China Sea is seen in run *G1d_echam5_20c* (Fig. 15(b)), but is absent in the *G1d_Mk3.5_20c* run (Fig. 15(d)). The CCAM forced runs suggest a stronger relationship between H_{Sm} anomalies and SOI in the Atlantic and Indian Oceans than observed in the *G1d_ncfsr* run (Fig. 15(a)) or implied by previous studies. In the Indian Ocean, the positive correlation on Australia's west coast continues westward across the basin, reaching a maximum along the African coast. A strong positive relationship to the SOI is observed in the North Atlantic which is not observed in existing data.

Runs *G1d_echam5_21c* and *G1d_Mk3.5_21c*, representing the end of 21st century under the A2 future emission scenario, show H_{Sm} anomalies correlate with SOI similarly to the current climate, but several significant differences are noted (Fig. 15(c) and (e)). While strong negative relationships are observed over large portions of the Pacific, we see changes in distribution. In both model run sets, we see a significant weakening of the negative relationships in the western north-equatorial region, and a significant strengthening the positive correlation to SOI is observed in the adjacent South China Sea in the *G1d_echam5_21c* (*G1d_Mk3.5_21c*) results. The negative regression coefficients in the south-west equatorial Pacific and the northern westerly storm belt have both weakened, becoming less negative towards the end of the 21st century. A region of significant positive correlation is observed adjacent the Alaskan coast which was unobserved in either of the 20th century CCAM forced runs (*G1d_echam5_20c* and

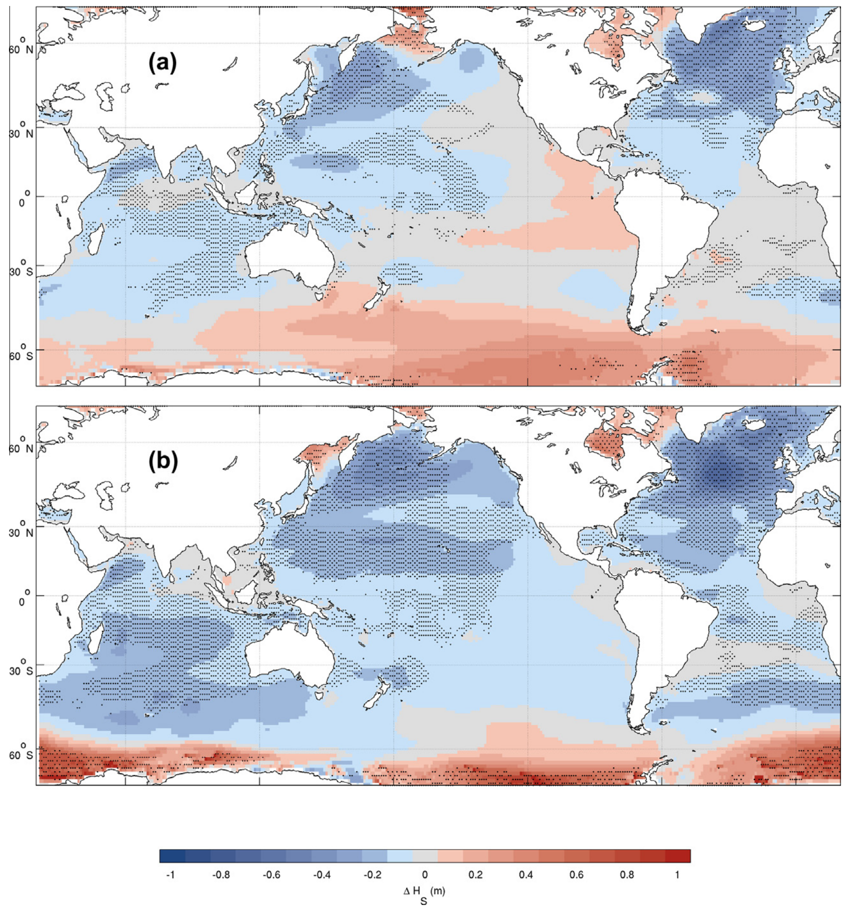

Fig. 12. Projected change (m) in annual mean significant wave height, H_S (2070–2099 less 1979–2009) for the SRES A2 scenario, from runs (a) *G1d_echam5_{20c,21c}*, (b) *G1d_mk3.5_{20c,21c}*. Only regions where the projected wave heights are significantly different to the present wave climates, at a 95% CI, are coloured. Stippling denotes regions where the magnitude of projected change exceeds the model bias. (For interpretation of the references to colour in this figure legend, the reader is referred to the web version of this article.)

G1d_Mk3.5_20c). The positive correlation in the south-east Pacific has also weakened in both runs. In the *G1d_echam5_20c* run particularly, the zonal extent is restricted considerably in the 21st century scenario. Whereas this positive relationship extended across the Pacific in runs *G1d_ncfsr* and *G1d_echam5_20c*, it is limited to being eastward of 240°E in run *G1d_echam5_20c* (Fig. 15(c)). The positive relationships in the Coral and Tasman Seas show a significant strengthening in the 21st century scenario from run *G1d_echam5_21c* (Fig. 15(c)), with the positive relationship shifting towards the Australian coast. In run *G1d_Mk3.5_21c*, a significant weakening of the positive relationship is seen in this region (Fig. 15(e)). The positive relationship observed across the Indian Ocean in *G1d_Mk3.5_20c* has significantly increased in the future CSIRO Mk3.5 forced scenario, but remains relatively unchanged in the ECHAM5 forced runs. However, the relationship to SOI in the Atlantic Ocean noted from the present climate runs are observed to have weakened in both run-sets.

The regression coefficients of the interannual H_{Sm} anomalies against the NAO for run *G1d_ncfsr* display a strong signal in the North Atlantic, consistent with previous studies (e.g., Woolf et al., 2002; Fig. 16(a)). The positive phase of the NAO is accompanied by an increase in wave heights in the North Atlantic between the United Kingdom and Greenland of up to approximately 4 cm per unit NAO (i.e., for a maximum NAO value of approximately 10 – see Table 2 – a 40 cm increase in annual mean H_{Sm} may be attributed to this relationship), and a decrease in wave heights further south stretching across all North Atlantic latitudes. This association is well documented, as occurring during a strengthening of the Icelandic low and Azores high pressure systems, leading to a strengthening of the North Atlantic storm track with consequent influence on the North Atlantic wave climate.

Fig. 16(b) and (d) shows the regression coefficients of the *G1d_echam5_20c* and *G1d_Mk3.5_20c* derived wave height anomalies relative to the NAO respectively, representing relationships in the current climate from the CCAM forced models. The strong dipole signal in the North Atlantic is observed in both runs, consistent with *G1d_ncfsr* and previous studies. A meridional dipole signature is similarly observed in the North Pacific in these runs, which suggests a strong Pacific teleconnection, not seen in existing observational datasets. Osborn (2004) showed the SLP patterns associated with the principal component of Atlantic sector SLP in the ECHAM4 AOGCM follows an Arctic Oscillation type pattern, with a similar strong teleconnection to the North Pacific. The positive regression coefficients in the Southern Ocean observed in run *G1d_cfsr* are not reproduced in the CCAM forced runs.

Fig. 16(c) and (e) shows the relationships as derived from runs *G1d_echam5_21c* and *G1d_Mk3.5_21c* respectively. In both CCAM forced run-sets, we see significant change in the structure of the North Atlantic dipole relationship of wave height anomalies with the NAO. In the ECHAM5 derived runs (Fig 16(b) and (c)), a strong positive relationship is observed between the United Kingdom and Greenland, as observed in other datasets, but the negative correlation further southwards in the North Atlantic has weakened significantly, and a band of significant positive correlation is observed

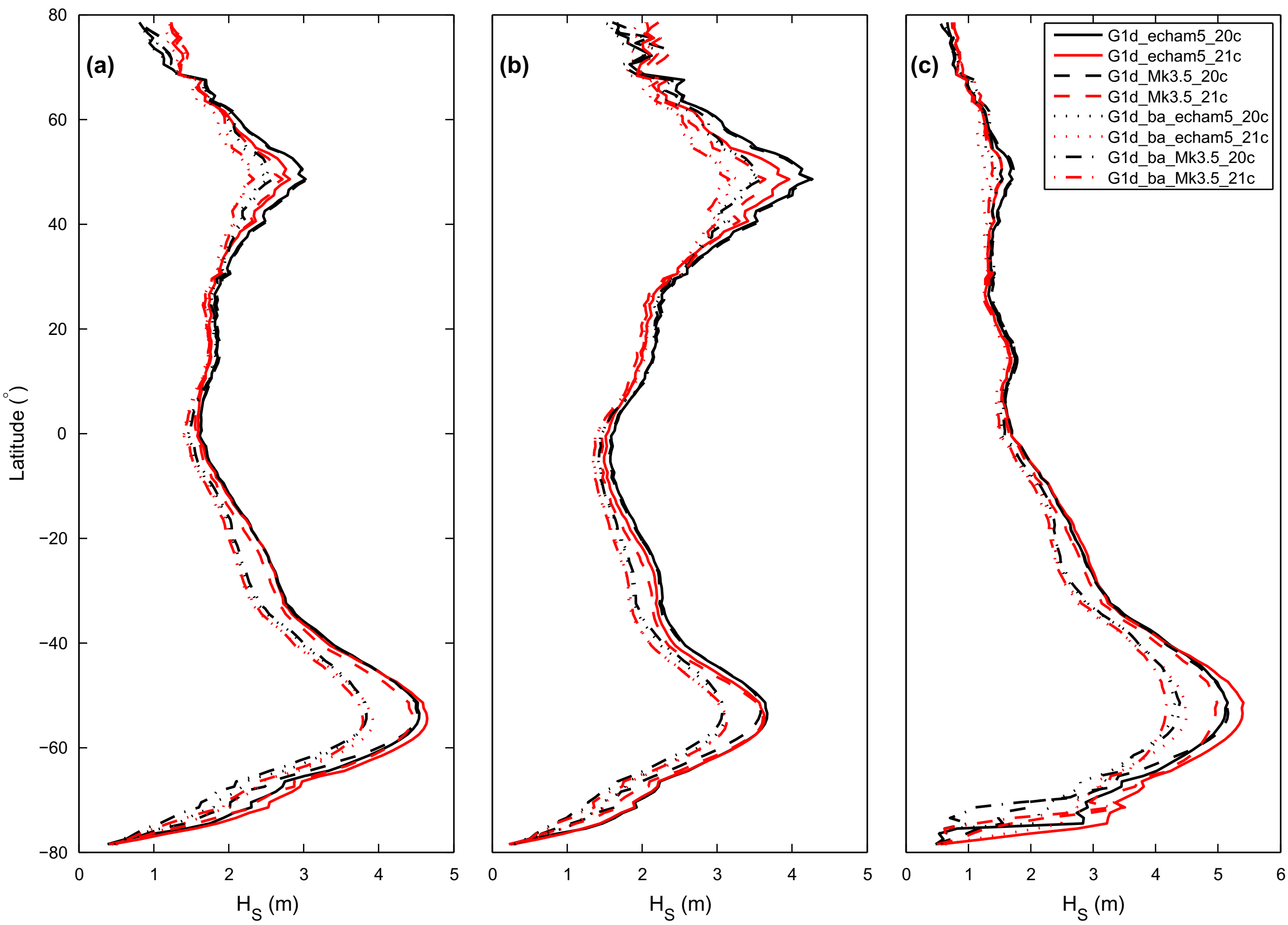

Fig. 13. Zonal mean significant wave height, H_S, for periods 1979–2009 and 2070–2099, from each climate model forced wave model run (m). (a) Annual mean, (b) Dec–Feb mean, and (c) Jun–Aug mean. Close agreement between respective CCAM forced models is observed by overlaying lines.

along the full length of the western European and north-west African coasts. In the CSIRO Mk3.5 derived runs (Fig. 16(d) and (e)), the strong positive relationship shows significant strengthening in the 21st century scenario, with significant positive relationships observed along the north-west European coast and Bay of Biscay. The Pacific teleconnection observed in the present climate run is also observed in the future climate.

The *G1d_ncfsr* wave climate displays a strong relationship between the H_{Sm} anomalies and the SAM (Fig. 17(a)). A positive SAM phase is associated with a positive anomaly of wave heights in the Southern Ocean, particularly the Pacific sector, and northwards into swell dominated regions of the eastern equatorial Pacific. In the Southern Ocean, we see a maximum regression coefficient of approximately 3 cm per SAM unit. This suggests that a strongly positive SAM phase (value of approximately 10 – see Table 2) is accompanied by an increase of approximately 30 cm in annual mean H_{Sm} in this region. Accompanying the positive relationship in the far Southern Ocean is a negative relationship in the extratropics southwest of Australia and in the South Atlantic, consistent with the southern shift in position of the southern storm belt associated with a positive phase of SAM. These features were reported by Hemer et al. (2010a) from both altimeter derived wave height data and the ERA-40 reanalysis wave data.

The *G1d_echam5_20c* and *G1d_Mk3.5_20c* runs display similar relationships between H_{Sm} anomalies and the SAM (Fig. 17(b) and (d)), with a strong positive correlation in the Southern Ocean, extending northwards into the swell dominated region of the eastern equatorial Pacific, and a negative correlation in the southern extratropics. A strong relationship between SAM and H_{Sm} anomalies in the Southern Ocean is also observed in the future projected wave climate (*G1d_echam5_21c* and *G1d_Mk3.5_21c*; Fig. 17(c) and (e)), although significantly weaker relative to the current climate time-slice over most longitudes in both run-sets. The negative relationship observed in the southern extratropics for the present climate is also much weaker in the future climate in both run-sets, particularly in the Indian Ocean, suggesting an overall weakening of the H_S relationship to SAM variability in the future time-slice.

5. Discussion and conclusions

A global 1° resolution implementation of a third generation wave model, WaveWatch III (v3.14), has been run for two 30-yr time-slices: One time-slice representing the current climate, and another representing a future climate scenario under the IPCC SRES A2 emission scenario. Forcing winds (and sea-ice fields) were derived from two CMIP-3 global climate model runs (ECHAM5 and CSIRO Mk3.5), which were dynamically downscaled using the Cubic Conformal Atmospheric Model to 0.5° spatial resolution, with 3-hourly temporal archives. Wave model runs were also carried out using forcing winds taken from the CCAM downscaling runs, with further bias-adjustment of the wind fields to align their distribution with the NCEP Climate Forecast System Reanalysis (using the method proposed by Hemer et al., 2012a). The wave climate obtained using climate model forcing was compared to the wave

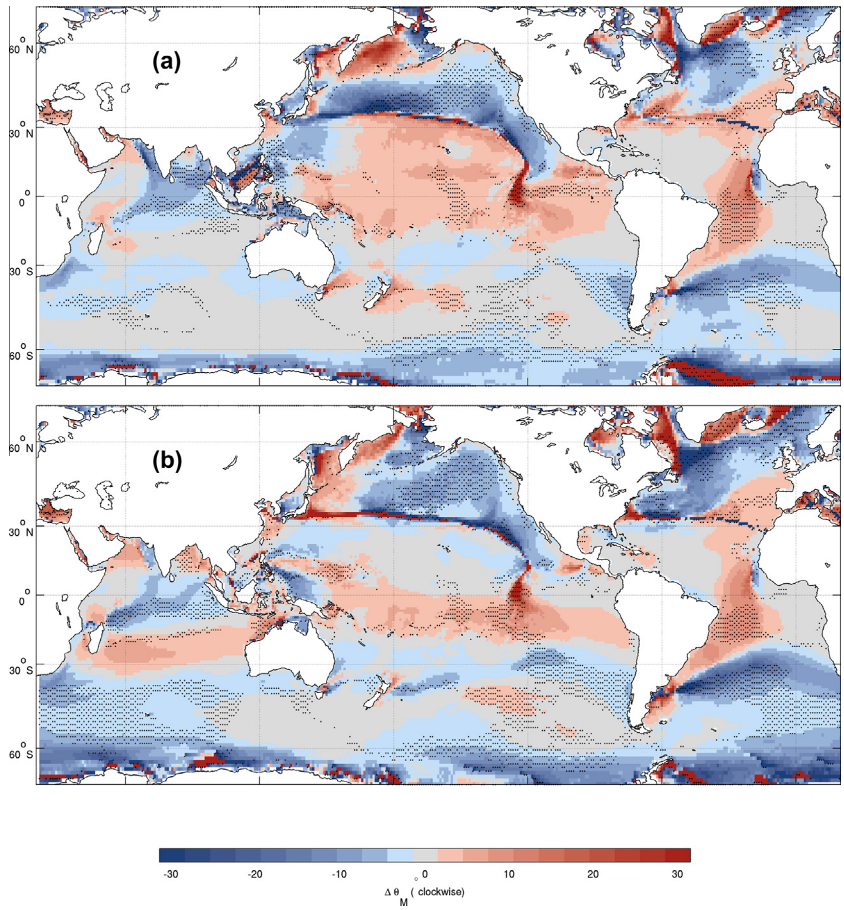

Fig. 14. Projected change (°clockwise) in annual mean wave direction, m (2070–2099 less 1979–2009) for the SRES A2 scenario, from runs (a) *G1d_echam5_{20c,21c}*, (b) *G1d_mk3.5_{20c,21c}*. Only regions where the projected wave directions are significantly different to the present wave climates, at a 95% CI, are coloured. Stippling denotes regions where the magnitude of projected change exceeds the model bias. (For interpretation of the references to colour in this figure legend, the reader is referred to the web version of this article.)

climate obtained when WaveWatch III was forced with NCFSR winds, under the same model settings.

The NCFSR forced WaveWatch III wave model displays notable biases relative to the ERA-Interim derived wave climate, when using default BAJ parameterisation in the model. The BAJ parameterisation was chosen after an initial 1-yr run with this parameterisation which showed better validation against ERA-Interim relative to a 1-yr run with the default WaveWatch III settings using Tolman and Chalikov (1996) source term parameterisations. Increased resolution of the NCFSR winds are a probable cause of the positive biases observed in model derived wave heights, particularly in the Southern Ocean. We did not tune WaveWatch III parameters to improve model skill with NCFSR forcing. Recently completed wave model hindcasts using NCFSR winds with a new source term parameterisation (Ardhuin et al., 2010, 2011) within WaveWatch III indicate model skill can be improved using the same forcing. Despite the biases observed between the *G1d_cfsr* derived wave heights from this study and ERA-Interim fields, the *G1d_cfsr* run provides a valuable control for climate model forced wave runs, where model differences can be isolated, with the only difference between models being surface wind forcing and sea ice extent.

The climate model forced wave model runs produce a wave climate qualitatively consistent with previous studies. Relative to the *G1d_cfsr* run, the direct climate forced wave fields show positive biases in H_{Sm} in the Southern Ocean of approximately 0.25 m, and a negative bias of similar magnitude in the North Pacific. The climate model winds have a general bias toward an exaggerated zonal circulation (extratropical westerlies and trade winds are overestimated in magnitude, with a directional bias towards zonal flow). These characteristics are similarly transferred to the simulated wave climate. However, we also see a positive bias in H_{Sm} in regions where swell generated in the Southern Ocean has propagated, associated with the overestimate of Southern Ocean wave heights (and underestimate of North Pacific wave heights) in these runs.

Aiming to improve the biases in the simulated wave field, each set of CCAM derived winds (CCAM-ECHAM5 and CCAM-CSIRO-Mk3.5) were bias-adjusted so that the bivariate surface wind distributions in the 1979–2009 time-slice aligns with the NCFSR wind distribution at any given point. The mean significant wave heights in the Southern Ocean show improvement relative to ERA-Interim when forced with the bias-adjusted CCAM winds, but a negative bias with respect to the benchmark *G1d_cfsr* run. The reduced bias relative to ERA-Interim, but large (negative) biases relative to the control *G1d_cfsr* run indicate the bias-adjustment has not improved model skill (when compared in a consistent model space). Furthermore, large negative biases (relative to *G1d_cfsr* and ERA-Interim) in the storm wave statistic used in this study (H_{Sm99}) are observed in these runs with bias-adjusted wind forcing. In their east Australian regional wave climate study, Hemer et al. (2012a) reported a decrease in the performance of the model to represent storm wave statistics after bias-adjustment of forcing winds, but argued that the increased model skill in representing the mean wave climate justified use of the proposed bias-adjustment

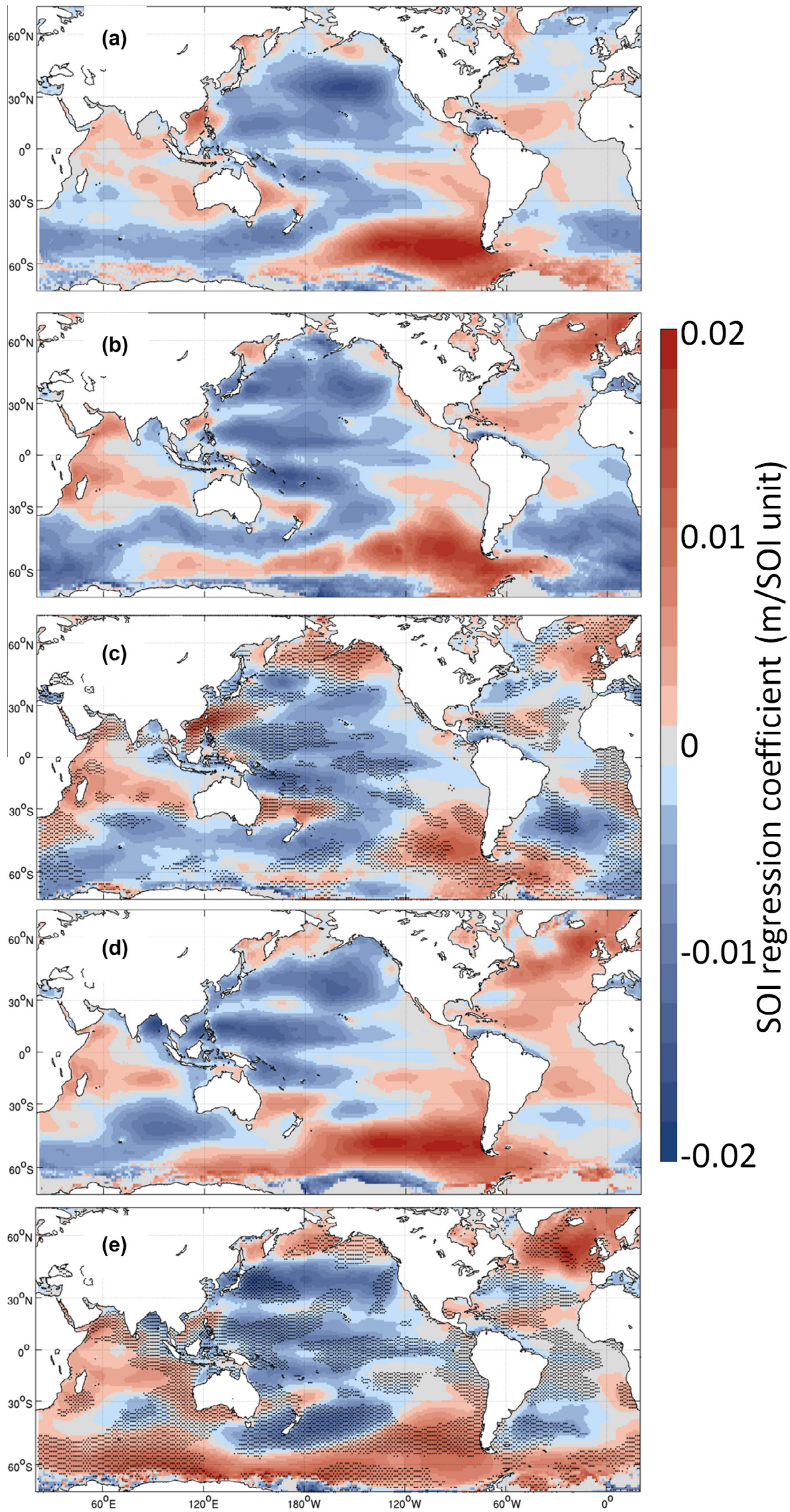

Fig. 15. Regression coefficient of the 12 month running mean of the mean H_S anomaly (after annual cycle removed) against the 12 month running mean of the Southern Oscillation Index. (a) *G1d_cfsr*, (b) *G1d_echam5_20c*, (c) *G1d_echam5_21c*, (d) *G1d_Mk3.5_20c*, and (e) *G1d_Mk3.5_21c*. Stippled regions have a significantly different regression coefficient (at 95% confidence level) in the projected future run. Only regions with correlation significant at 95% level are coloured. See Table 2 for range of SOI values in our study. (For interpretation of the references to colour in this figure legend, the reader is referred to the web version of this article.)

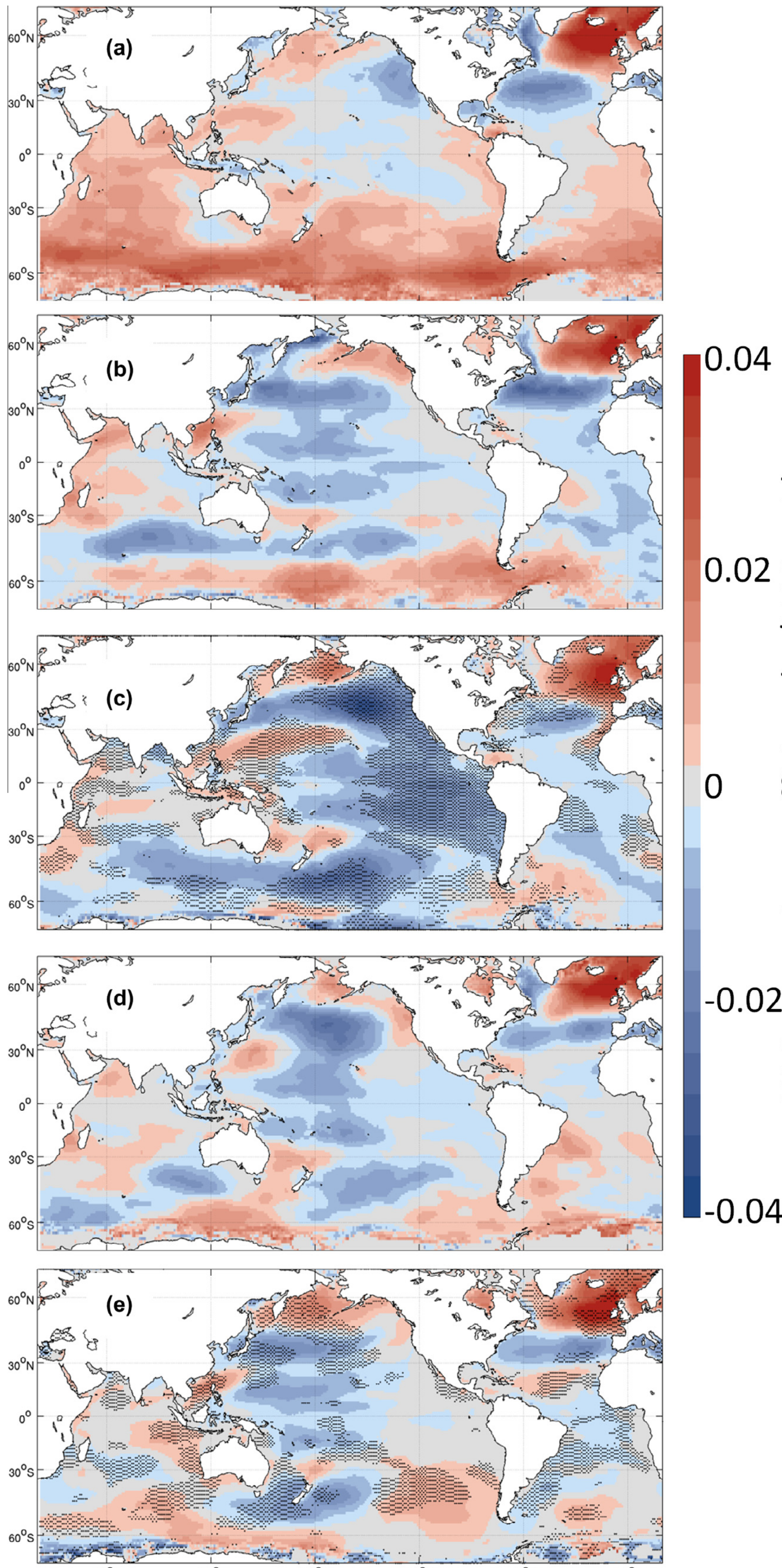

Fig. 16. Regression coefficient of the 12 month running mean of the mean H_S anomaly (after annual cycle removed) against the 12 month running mean of the North Atlantic Oscillation. (a) *G1d_cfsr*, (b) *G1d_echam5_20c*, (c) *G1d_echam5_21c*, (d) *G1d_Mk3.5_20c*, and (e) *G1d_Mk3.5_21c*. Stippled regions have a significantly different regression coefficient (at 95% confidence level) in the projected future run. Only regions with correlation significant at 95% level are coloured. See Table 2 for range of SOI values in our study. (For interpretation of the references to colour in this figure legend, the reader is referred to the web version of this article.)

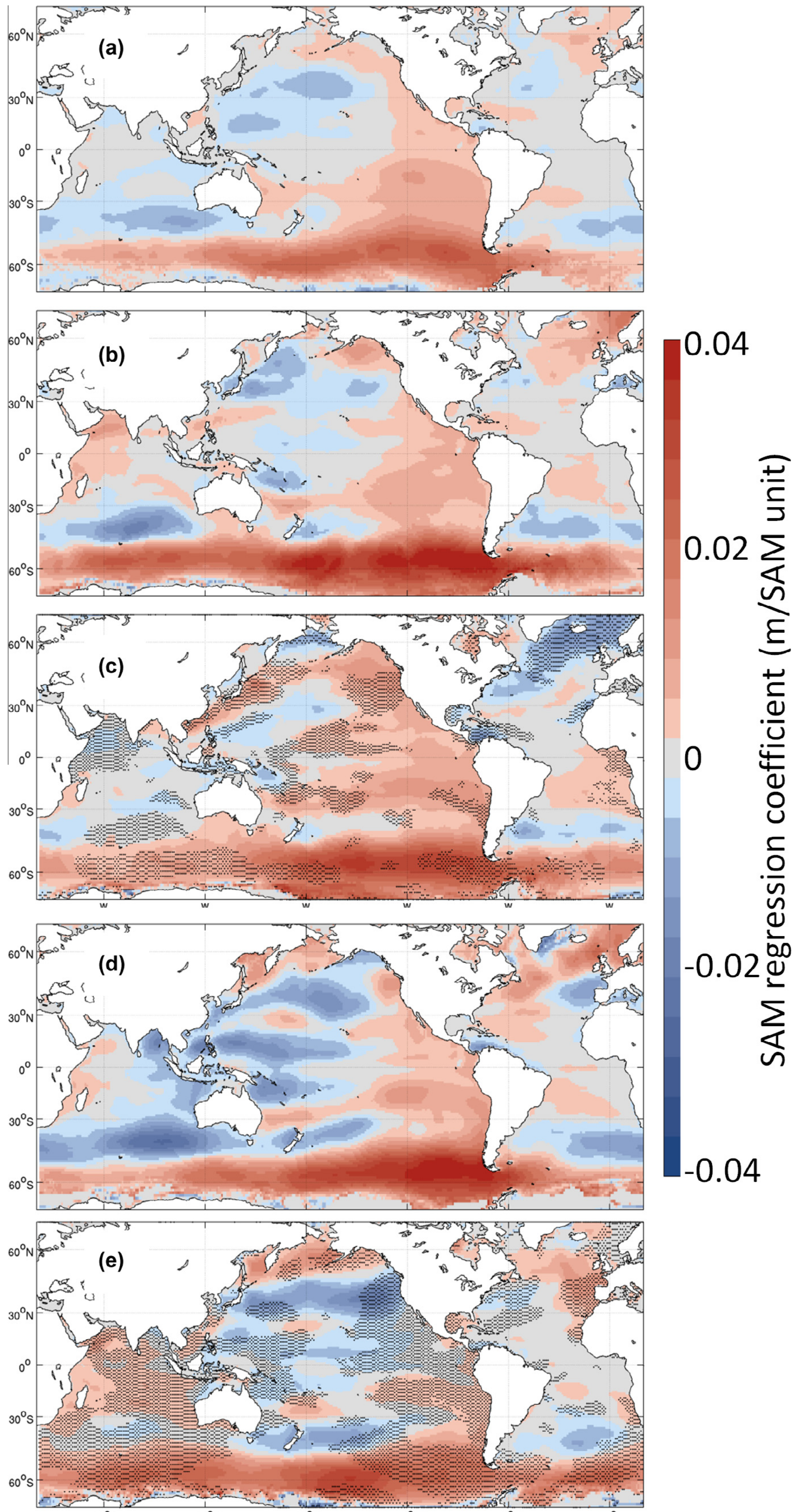

Fig. 17. Regression coefficient of the 12 month running mean of the mean H_S anomaly (after annual cycle removed) against the 12 month running mean of the Southern Annular Mode Index. (a) *G1d_cfsr*, (b) *G1d_echam5_20c*, (c) *G1d_echam5_21c*, (d) *G1d_Mk3.5_20c*, and (e) *G1d_Mk3.5_21c*. Stippled regions have a significantly different regression coefficient (at 95% confidence level) in the projected future run. Only regions with correlation significant at 95% level are coloured. See Table 2 for range of SOI values in our study. (For interpretation of the references to colour in this figure legend, the reader is referred to the web version of this article.)

Table 2
Minimum and maximum values of climate indices in each dataset, defining the range, according to definition used in this study.

		Historical (1979–2009)		Future (2070–2099)	
		Min	Max	Min	Max
SOI	NCFSR	−18.4	8.9	–	–
	ECHAM5	−16.6	14.7	−15.6	10.9
	Mk3.5	−13.2	18.0	−13.4	12.7
NAO	NCFSR	−4.2	6.2	–	–
	ECHAM5	−7.5	11.1	−8.5	10.2
	Mk3.5	−8.2	8.5	−10.3	10.5
SAM	NCFSR	−7.4	8.8	–	–
	ECHAM5	−13.9	8.2	−8.5	10.2
	Mk3.5	−8.0	9.1	−8.7	10.5

method. In this global study, we find that bias-adjustment of the forcing winds has marginal influence on the wave height distribution up to approximately the upper end of the inter-quartile range, but deteriorates model performance of storm wave conditions to a level where we do not support application of this procedure. The method used is a bivariate adjustment of the distribution of eastward and northward wind components from the climate model, to align with the distribution from the reanalysis. Wang et al. (2010) show that adjustment of mean wind speed leads to improvement of the dynamically derived wave field, but suggested further improvements are likely possible. The procedure used in this study reduces model skill to represent the storm wave climate. One cause of this is likely the bivariate-quantile-adjustment resulting in too few samples at storm wind speeds for given directions to construct a satisfactory adjustment matrix. Improvement may be achieved by adjusting wind-stresses (instead of speeds), which would adjust the forcing stresses, however the problem of sparse sampling at wind speed extremes for given directions would remain. Given directional wind biases are typically within the relatively coarse directional resolution of the global wave models (15°), a quantile adjustment of wind speed (or wind stress magnitude) may be sufficient to improve the simulated wave climate, overcoming the shortcomings of the present method. This study, by deterioration of storm wave climate fields after bias-adjustment of wind fields has been carried out, has demonstrated that adjustment of the upper percentiles of climate model derived wind speeds (in this study limited by 98th percentile) requires independent study. Another alternative to improve wave climate model fields would be to apply a bias adjustment to the output wave fields themselves, as applied by Charles et al. (2012). Trials of different bias-adjustment procedures are ongoing, which also includes assessment of the best approaches to ensure high percentiles (storm wave conditions) are best represented.

Projected changes in wave climate for the given future emission scenario (SRES A2) are relatively insensitive to whether bias-adjustment of wind forcing is carried out. Two strong robust signals are observed in the projected changes in both CCAM model sets. Firstly, an increase in Southern Ocean wind speeds transfers to generation of larger waves in the region. These Southern Ocean generated wave systems are observed to propagate northwards into the other ocean basins, so that corresponding increases in significant wave height (H_{Sm} and H_{Sm99}) and mean wave period are observed, with an increase in the contribution of southerly waves to the wave spectrum in these regions, shifting the projected mean wave direction to a more southerly orientation. The second feature which is common to both CCAM model run sets is a decrease in wind speeds in the North Atlantic, with a corresponding decrease in significant wave heights and wave periods in the region. Wave direction responds to future change in the region with a divergence, so that south-westerly waves in the north have an increasing southerly component, and west-south-westerly waves nearer to the west European coast have an increasing westerly, or northerly, component. A similar decrease in wave heights and periods is observed in the North Pacific, but not as strong or as consistent between the two models.

Our 'ensemble' is small, with only two downscaled GCMs having been considered for a single emission greenhouse gas emission scenario. We recognise that our sample is extremely limited within the total sample space which surrounds projections of wave climate. Several sources of uncertainty surround wave climate projections, consisting of the future emission scenario, GCM, GCM parameterisation, downscaling methodology, and the method used to determine the projected wave field (including both dynamical and statistical approaches). The results of this study must therefore be considered within the context of other studies which have investigated projected future changes in wave climate. Wang and Swail (2006) developed statistical projections of the surface wind wave climate from three GCMs for three forcing scenarios, exploiting the statistical relationship between mean sea level pressure and/or surface winds and the surface wind wave climate. Statistical projections have the advantage of being computationally inexpensive, and not requiring sub-daily wind-fields, but in studies carried out so far are limited to projections of significant wave height only. Mori et al. (2010) used surface winds derived from the 20 km resolution Japanese Meteorological Research Institute and Japan Meteorological Agency (MRI/JMA) GCM, forced using an ensemble mean SST obtained from the ensemble of CMIP3 GCMs, to force a global implementation of the SWAN model, for an SRES A1B scenario. Quantitative inter-comparisons of the results from this study and these other studies is underway, as a contribution of the Coordinated Ocean Wave CLImate Projections project (Hemer et al., 2012c), but qualitatively, we see strong similarities between these studies, with projected increase of approximately 10% in mean Southern Ocean mean wave heights, and projected decrease of up to 15% in mean wave heights in the central North Atlantic.

In this study, we have assessed only changes in integrated wave parameters, H_S, T_M and θ_M, with various inferences on how this has influenced sea and swell components of the wave field. Given the spatial variability of projected change in the surface wave field, sea and swell components of the wave field at any location will be independent of one another. Our model has archived the full modelled wave spectrum at many locations across the global ocean, and partitioned sea and swell fields at all locations. Ongoing analysis will assess how the surface wave spectrum across the global ocean responds to the projected future climate scenario.

It is now well established that modes of variability of the wider climate system are equally observed in the wave climate. For example, strong relationships are observed between the Pacific wave climate and climate indices associated with ENSO. In the North Atlantic, significant relationships between wave parameters and the NAO are observed, and the principal mode of variability of wave climate in the Southern Hemisphere is significantly correlated to the SAM. In this study, the relationship between wave climate and the climate indices mentioned above have been investigated, but it could be expected that relationships to several other indices (e.g., Pacific Decadal Oscillation, Arctic Oscillation, Indian Ocean Dipole) exist. However, it is not clear whether the relationships between interannual variability of the wave climate and these indices are robust in a changing climate. We have investigated the relationship between H_{Sm} and the SOI, NAO and SAM from the simulated present and future wave climates. Maps of correlation of these indices at a seasonal level, and with T_{Mm} and θ_{Mm} would provide further insight on potential shifts in wave generation areas, but is left to a following study.

While there has been steady progress in the skill of simulating ENSO within AOGCMs, systematic errors remain which limit the ability of the models to reproduce the mean climate and natural variability (Randall et al., 2007). Most models do not capture the full meridional extent of the sea-surface temperature (SST) anomalies in the eastern Pacific, and tend to produce anomalies which extend too far into the western Pacific. Many models produce ENSO variability which occurs on time-scales much faster than observed (Randall et al., 2007). Future projections in the tropical Pacific Ocean under enhanced greenhouse gas emissions suggest a general increase in SST, with a greater increase over the eastern tropical Pacific than over the western tropical Pacific, together with a decrease in SLP gradient along the equator and an eastward shift of the tropical Pacific rainfall distribution. This has been described as an El Niño-like mean state change (upon which individual ENSO events occur, Meehl et al., 2007). Each model, however, shows differing projected response of El Niño variability. ECHAM5 and CSIRO Mk3.0 (a predecessor of CSIRO Mk3.5) were noted as two models which, along with the majority of models, project a shift towards a more El Niño like mean state. While ECHAM5 suggested a slight increase in El Niño variability under enhanced greenhouse gases, CSIRO Mk3.0 displayed little change (Meehl et al., 2007). In our two datasets, regression coefficients between H_S anomaly and SOI show significant differences in the future time-slice, relative to the present climate time-slice, over large portions of the Pacific domain. Regions of negative correlation show a significant weakening relationship to the SOI, most notable in the northern west equatorial Pacific. Regions of positive correlation in the South China Sea show a significant strengthening, suggesting the known ENSO response of wave conditions will strengthen in a future climate, with broad associated implications in these regions. In the Tasman Sea, the results from the two models diverge, with ECHAM5 derived runs showing a projected significant increase in the positive relationships in the region, whereas the CSIRO Mk3.5 derived runs project a significant weakening. These results demonstrate the difficulty of working from just two climate model runs, and the need to increase our future ensemble of projected wave climate change scenarios.

A strong relationship between wave height anomalies and the NAO is observed in the North Atlantic in both our present and projected wave climate simulations. The IPCC fourth assessment report indicated the AOGCM multi-model ensemble is capable of reproducing many aspects of the NAO (Randall et al., 2007, IPCC Ch.8). Many of the models project a decrease in arctic MSLP in the 21st century, which would result in an increasing trend in the NAO, as suggested by more than half of the models (Randall et al., 2007). Neither ECHAM5 or CSIRO Mk3.5 were part of the model ensemble from which this study was taken, but their predecessors ECHAM4 and CSIRO Mk2 were typical of models which bounded the ensemble – ECHAM4 suggesting a large positive trend in the NAO into the 21st century, and CSIRO Mk2 suggesting no future trend (Osborn, 2004). North Atlantic wave heights are projected to decrease under the future climate scenario, but the relationship to the NAO in the region is more complex. We see significant changes in the relationship between the NAO and H_S anomalies in the region, particularly in the Bay of Biscay (from both models), and extending as far south as the north-west African coast in the ECHAM5 derived runs. In locations where a positive phase of the NAO is associated with negative H_S anomalies in the present climate, we see the positive phase of the NAO is accompanied by positive H_S anomalies in the future climate. Regions of negative anomalies display a shift offshore into the central Atlantic. This response suggests while wave heights decrease in the projected climate, there is an increasing influence of a swell component from waves generated further north in this region during positive NAO phases. This response is consistent with the clockwise rotation of wave direction in this region, seen in our simulations, and also reported from regional studies (Charles et al., 2012).

The present and projected wave climates derived from our simulations display strong positive relationships over large portions of the Southern Hemisphere between the SAM and H_{Sm} anomalies. The spatial structure of the SAM is well represented within the CMIP multi-model ensemble (Randall et al., 2007). However discrepancies exist in amplitude, the detailed zonal structure and the temporal structure. For example, Randall et al. (2007) showed that the ECHAM5 modelled SAM variance was almost twice as large as the SAM variance within the NCEP reanalysis. While ozone recovery is expected to lead to a reversal in the SAM response in future austral summers (Arblaster et al., 2011), poleward shifts in the southern extratropical storm track and a positive trend in the SAM are projected in almost all climate models under future high CO_2 scenarios (Meehl et al., 2007).

As we have seen with other indices, the relationship between H_S anomalies and the SAM shows significant differences between the present and projected climate simulations. A significant weakening in the negative relationship between SAM and H_S anomalies is observed in the southern extratropics, particularly in the Indian Ocean.

Researchers have proposed using relationships between wave climate and these indices to project future changes in wave climate. These statistical projections are based on an assumption of stationarity (identified relationships between present local variable and large-scale variable are assumed to be the same in the future climate, in the context of climate change). However, these significant differences in the relationships from one time-slice to another question this assumption and require consideration when aiming to reconstruct wave climate from projected changes in SOI, NAO and/or SAM (or other climate index).

This study has presented global dynamical projected changes in wave climate for a single high emission scenario, SRES A2, from two GCMs. Significant changes in wave climate are projected over large regions of the global ocean, and it can be expected that such changes may impact a range of activities and processes in a future warmer climate. Surface waves drive coastal circulations, influence coastal ecosystems, drive transport of coastal and nearshore sediments and hence influence shoreline stability, and are capable of causing considerable damage to offshore and coastal infrastructure. While there is evidence that the influence of a changing wave climate may dominate the influence of sea-level rise in some coastal regions (e.g., Coelho et al., 2009), it could be expected that in some locations, the combined influence of these non-stationary processes will likely be greater, with dramatic effects in the coastal zone. Much future research is required to first quantify, but ultimately narrow, the uncertainties which surround projected future changes in wave climate on global scales (see Hemer et al., 2012c), and furthermore, to apply these to local-scale studies to comprehend the consequent impacts. The availability of CMIP5 experiments (Taylor et al., 2012) provides a much improved dataset (high spatial and temporal resolution) to support wave climate projection studies, and we continue to assess the influence of projected future changes in atmospheric circulation on wave climate with these new scenarios. However, it must be recognised that while future impacts of wave climate change will be highly variable on the basis of the magnitude of projected change, the adaptive capacity of the coast or industry/activity being considered will also play a critical role.

Acknowledgements

This manuscript is a contribution of the Climate Variability and Change Programme of the Centre for Australian Weather and Climate Research: A Partnership between CSIRO and the Bureau of Meteorology. We acknowledge the modelling groups, the Program for Climate Model Diagnosis and Inter-comparison (PCMDI) and the WCRP's Working Group on Coupled Modelling (WGCM) for their roles in making available the WCRP CMIP3 multi-model dataset. Support of this dataset is provided by the Office of Science, U.S. Department of Energy. We acknowledge the European Centre for Medium Range Weather Forecasts (ECMWF) for providing ERA-Interim wave reanalysis data to the research community, and NOAA's National Centers for Environmental Prediction (NCEP) for the CFSR data. We also acknowledge support from CSIRO's Wealth from Oceans National Research Flagship, and the Pacific Australia Climate Change Science and Adaptation Program (PACCSAP). We thank Dr's Elodie Charles and Kathleen McInnes for helpful comments and discussions on earlier versions of the manuscript.

References

Allan, J.C., Komar, P.D., 2006. Climate controls on US West Coast erosion processes. Journal of Coastal Research 22 (3), 511–529.

Arblaster, J.M., Meehl, G.A., Karoly, D.J., 2011. Future climate change in the Southern Hemisphere: competing effects of ozone and greenhouse gases. Geophysical Research Letters 38, L02701. http://dx.doi.org/10.1029/2010GL045384.

Ardhuin, F., Rogers, E., Babanin, A.V., Filipot, J.-F., Magne, R., Roland, A., van der Westhuysen, A., Queffeulou, P., Lefevre, J.-M., Aouf, L., Collard, F., 2010. Semiempirical dissipation source functions for ocean waves. Part I: definition, calibration, and validation. Journal of Physical Oceanography 40, 1917–1941.

Ardhuin, F., Hanafin, J., Quilfen, Y., Chapron, Y., Queffeulou, P., Obrebski, M., Sienkiewicz, J., Vandermark, D., 2011. Calibration of the IOWAGA Global Wave Hindcast (1991–2011) using ECMWF and NCFSR winds. In: 12 International Workshop on Wave Hindcasting and Forecasting, Hawaii, 2011. Available from: <http://www.waveworkshop.org/12thWaves/papers/Ardhuin_etal_hindcast_WHF2011.pdf>.

Bidlot, J.-R., Janssen, P., Abdalla, S., 2007. Impact of the revised formulation for ocean wave dissipation on the ECMWF operational wave model. Tech. Memo. 509, ECMWF: Reading, UK.

Cavaleri, L., Fox-Kemper, B., Hemer, M., 2012. Wind-waves in the coupled climate system. Bulletin of the American Meteorological Society. http://dx.doi.org/10.1175/BAMS-D-11-00170.1.

Charles, E., Idier, D., Delecluse, P., Deque, M., Le Cozannet, G., 2012. Climate change impact on waves in the Bay of Biscay. Ocean Dynamics 62 (6), 831–848, http://dx.doi.org/10.1007/s10236-012-0534-8.

Chawla, A., Tolman, H., 2007. Automated grid generation for WAVEWATCH III. NOAA / NWS / NCEP / MMAB Technical Note 254, 71 pp.

Coelho, C., Silva, R., Veloso-Gomes, F., Taveira-Pinto, F., 2009. Potential effects of climate change on northwest Portuguese coastal zones. ICES Journal of Marine Science 66, 1497–1507.

Cox, A., Cardone, V., Swail, V., 2011. On the use of the climate forecast system reanalysis wind forcing in ocean response modeling. In: 12th International Workshop on Wave Hindcasting and Forecasting, Hawaii, 2011. Available from: <http://www.waveworkshop.org/12thWaves/papers/On the Use of the Climate Forecast System Reanalysis Wind Forcing in Ocean Response Modeling.pdf>.

Dee, D.P., Uppala, S.M., Simmons, A.J., Berrisford, P., Poli, P., Kobayashi, S., Andrae, U., Balmaseda, M.A., Balsamo, G., Bauer, P., Bechtold, P., Beljaars, A.C.M., van de Berg, L., Bidlot, J., Bormann, N., Delsol, C., Dragani, R., Fuentes, M., Geer, A.J., Haimberger, L., Healy, S.B., Hersbach, H., Hólm, E.V., Isaksen, L., Kållberg, P., Köhler, M., Matricardi, M., McNally, A.P., Monge-Sanz, B.M., Morcrette, J.-J., Park, B.-K., Peubey, C., de Rosnay, P., Tavolato, C., Thépaut, J.-N., Vitart, F., 2011. The ERA-Interim reanalysis: configuration and performance of the data assimilation system.. Quarterly Journal of the Royal Meteorological Society 137, 553–597. http://dx.doi.org/10.1002/qj.828.

Efron, B., 1982. The jackknife, the bootstrap, and other resampling plans. Society of Industrial and Applied Mathematics CBMS-NSF Monographs, vol. 38. ISBN 0-89871-179-7.

Fan, Y., Lin, S.-J., Held, I., Yu, Z., Tolman, H., in press. Global Ocean Surface Wave simulation using a coupled atmosphere–wave model. Journal of Climate 25, 6233–6252. http://dx.doi.org/10.1175/JCLI-D-11-00621.1.

Gulev, S.K., Grigorieva, V., 2004. Last century changes in ocean wind wave height from global visual wave data. Geophysical Research Letters 31, L24302. http://dx.doi.org/10.1029/2004GL021040.

Harley, M.D., Turner, I.L., Short, A.D., Ranasinghe, R., 2011. A reevaluation of coastal embayment rotation: the dominance of cross-shore versus alongshore sediment transport processes, Collaroy-Narrabeen Beach, southeast Australia. Journal of Geophysical Research 116, F04033. http://dx.doi.org/10.1029/2011JF001989.

Hemer, M.A., Church, J.A., Hunter, J.R., 2010a. Variability and trends in the directional wave climate of the Southern Hemisphere. International Journal of Climatology 30, 475–491.

Hemer, M.A., Wang, X.L., Church, J.A., Swail, V.R., 2010b. Coordinating global ocean wave climate projections. Bulletin of the American Meteorological Society 91 (4), 451–454.

Hemer, M.A., Wang, X.L., Weisse, R., Swail, V.R., 2012a. Community advancing wind-waves climate science: the COWCLIP project. Bulletin of the American Meteorological Society 93 (6), 791–796. http://dx.doi.org/10.1175/BAMS-D-11-00184.1.

Hemer, M.A., McInnes, K., Ranasinghe, R., 2012b. Exploring uncertainty in regional east Australian wave climate projections. International Journal of Climatology. http://dx.doi.org/10.1002/joc.3537.

Hemer, M.A., McInnes, K.L., Ranasinghe, R., 2012c. Climate and variability bias adjustment of climate model-derived winds for a southeast Australian dynamical wave model. Ocean Dynamics 62 (1), 87.

IPCC, 2007. In: Solomon, S., Qin, D., Manning, M., Chen, Z., Marquis, M., Averyt, K.B., Tignor, M., Miller, H.L. (Eds.), Climate Change 2007: The Physical Science Basis. Contribution of Working Group I to the Fourth Assessment Report of the Intergovernmental Panel on Climate Change. Cambridge University Press, Cambridge, United Kingdom and New York, NY, USA.

Izaguirre, C., Mendez, F.J., Menendez, M., Luceño, A., Losada, I.J., 2010. Extreme wave climate variability in southern Europe using satellite data, Journal of Geophysical. Research 115, C04009, http://dx.doi.org/10.1029/2009JC005802.

Izaguirre, C., Méndez, F.J., Menéndez, M., Losada, I.J., 2011. Global extreme wave height variability based on satellite data. Geophysical Research Letters 38, L10607. http://dx.doi.org/10.1029/2011GL047302.

Katzfey, J.J., McGregor, J., Nguyen, K., Thatcher, M., 2011. The added value of dynamical downscaling. In: Proceedings of the 19th International MODSIM Congress, Perth, Australia, 12–16 July 2011, pp. 2747–2753. Available from: <http://www.mssanz.org.au/modsim2011/F5/katzfey.pdf>.

Laing, A.K., 2000. New Zealand wave climate from satellite observations. New Zealand Journal of Marine and Freshwater Research 34, 727–744.

McGregor, J.L., 2005. C-CAM: geometric aspects and dynamical formulation. CSIRO Marine and Atmospheric Research Technical Report 70. Available from: <http://www.cmar.csiro.au/e-print/open/mcgregor_2005a.pdf>.

McGregor, J.L., Dix, M.R., 2008. An updated description of the conformal-cubic atmospheric model. In: Hamilton, K., Ohfuchi, W. (Eds.), High Resolution Simulation of the Atmosphere and Ocean. Springer, Berlin, pp. 51–76.

Meehl, G.A. et al., 2007. Global climate projections. In: Solomon, S., Qin, D., Manning, M., Chen, Z., Marquis, M., Averyt, K.B., Tignor, M., Miller, H.L. (Eds.), Climate Change 2007: The Physical Science Basis. Contribution of Working Group I to the Fourth Assessment Report of the Intergovernmental Panel on Climate Change. Cambridge University Press, Cambridge, United Kingdom and New York, NY, USA.

Mori, N., Yasuda, T., Mase, H., Tom, T., Oku, Y., 2010. Projection of extreme wave climate change under the global warming. Hydrological Research Letters 4, 15–19. http://dx.doi.org/10.3178/hrl.4.15.

Osborn, T.J., 2004. Simulating the winter North Atlantic Oscillation: the roles of internal variability and greenhouse gas forcing. Climate Dynamics 22, 605–623.

Ranasinghe, R., McLoughlin, R., Short, A., Symonds, G., 2004. The Southern Oscillation Index, wave climate, and beach rotation. Marine Geology 204, 273–287.

Randall, D.A., Wood, R., Bony, S., Colman, R., Fichefet, T., Fyfe, J., Kattsov, V., Pitman, A., Shukla, J., Srinivasan, J., Stouffer, R., Sumi, A., Taylor, K., 2007. Climate models and their evaluation. In: Climate Change 2007: The Physical Science Basis. Contribution of Working Group I to the Fourth Assessment Report of the Intergovernmental Panel on Climate Change. Cambridge University Press, Cambridge, UK and New York, USA, pp. 589–662.

Saha, Suranjana et al., 2010. The NCEP climate forecast system reanalysis. Bulletin of the American Meteorological Society 91, 1015–1057. http://dx.doi.org/10.1175/2010BAMS3001.1.

Semedo, A., Sušelj, K., Rutgersson, A., Sterl, A., 2011. A Global view on the wind sea and swell climate and variability from ERA-40. Journal of Climate 24 (5), 1461–1479.

Short, A.D., Trembanis, A.C., 1994. Decadal scale patterns in beach oscillation and rotation Narrabeen Beach, Australia – Time Series, PCA and wavelet analysis. Journal of Coastal Research 20 (2), 523–532.

Short, A.D., Trembanis, A.C., Turner, I.L., 2000. Beach oscillations, rotation and the Southern Oscillation, Narrabeen Beach, Australia. In: Proceedings of the International Coastal Engineering Conference, Sydney, pp. 2439–2452.

Sterl, A., Caires, S., 2005. Climatology, variability and extrema of ocean waves: the web-based KNMI/ERA-40 wave atlas. International Journal of Climatology 25, 963–977.

Storlazzi, C.D., Griggs, G.B., 2000. The influence of El Niño-Southern Oscillation (ENSO) events on the evolution of central California's shoreline. Geological Society of America Bulletin 112 (2), 236–249.

Taylor, K., Stouffer, R., Meehl, G.A., 2012. An overview of 326 CMIP5 and the experiment design. Bulletin of the American Meteorological Society 93 (4), 485–498.

Thomas, T., Phillips, M.R., Williams, A.T., Jenkins, R.E., 2011. Short-term beach rotation, wave climate and the North Atlantic Oscillation. Progress in Physical Geography 35 (3), 333–352.

Tolman, H., 2009. User manual and system documentation of WAVEWATCH-III, version 3.14. NOAA/NWS/NCEP/MMAB Technical Note 276, 194 pp.

Tolman, H.L., Chalikov, D., 1996. Source terms in a third-generation wind-wave model. Journal of Physical Oceanography 26, 2497–2518.

Troup, A.J., 1965. The Southern Oscillation. Quarterly Journal of Royal Meteorological Society. 91, 490–506.

Wang, X.L., Swail, V.R., 2006. Climate change signal and uncertainty in projections of ocean wave heights. Climate Dynamics 26, 109–126. http://dx.doi.org/10.1007/s00382-005-0080-x.

Wang, X.L., Swail, V.R., Cox, A., 2010. Dynamical versus Statistical Downscaling Methods for Ocean Wave Heights. International Journal of Climatology 30 (3), 317–332. http://dx.doi.org/10.1002/joc.1899.

Weisse, R., von Storch, H., Callies, U., Chrastansky, A., Feser, F., Grabemann, I., Guenther, H., Pluess, A., Stoye, Th., Tellkamp, J., Winterfeldt, J., Woth, K., 2008. Regional meteo-marine reanalyses and climate change projections: results for Northern Europe and potentials for coastal and offshore applications. Bulletin of the American Meteorological Society 90, 849–860. http://dx.doi.org/10.1175/2008BAMS2713.1.

Woolf, D.K., Challenor, P.G., Cotton, P.D., 2002. Variability and predictability of the North Atlantic wave climate. Journal of Geophysical Research 107 (C10), 3145. http://dx.doi.org/10.1029/2001JC001124.

Young, I.R., 1999. Seasonal variability of the global ocean wind and wave climate. International Journal of Climatology 19, 931–950.

Young, I.R., Zieger, S., Babanin, A.V., 2011. Global trends in wind speed and wave height. Science 332, 451.